JOURNAL OF EXPERIMENTAL AND THEORETICAL PHYSICS, 2024, Vol. 166, No. 3 (9), pp. 331–356

SOLIDS AND LIQUIDS

POINT DEFECTS IN $FeMe_2O_4$ (Me = Fe, Cr) SPINELS: A DFT+U INVESTIGATION

© 2024 **G. D. Chichevatov** [a,b*], **V. V. Stegailov** [a,b,c]

[a] *Joint Institute for High Temperatures, Russian Academy of Sciences, 125412, Moscow, Russia*

[b] *Moscow Institute of Physics and Technology (National Research University), 141701, Dolgoprudny, Moscow region, Russia*

[c] *National Research University "Higher School of Economics", 101000, Moscow, Russia*

**e-mail: chichevatov.gd@phystech.edu*

Received April 02, 2024,
Revised April 02, 2024
Accepted April 21, 2024

Abstract. Spinel-type crystals AMe_2O_4 encompass a wide range of practical applications like photocatalysis or spintronics, but often demonstrate non-trivial electronic and magnetic properties which theoretical description is mitigated. In this work, we performed DFT+U calculations for the most extensive set of neutral point defects in Fe_3O_4 (magnetite) and $FeCr_2O_4$ (chromite) and investigated all the possible types of cationic and oxygen defects in both spinels. Our results unveil both similarities and principal differences between the defective Fe_3O_4 and $FeCr_2O_4$, posing chromite as a material less prone to defect formation, and could be a valuable asset to the development of new multiscale models of steel corrosion.

Keywords: *tmagnetite, chromite, first principles, Frenkel pair, steel corrosion*

DOI: 10.31857/S004445102409e062

1. INTRODUCTION

Accounting for strong electronic correlations in condensed matter modelling is one of the most pressing problems of modern physics. In many cases, this concerns transition metal compounds and, together with the presence of highly degenerate orbital degrees of freedom, leads to a wide variety of effects [1-3]. Some of these include phenomena of phase separation and charge ordering [4-6]. Magnetite Fe_3O_4 and some derivative iron oxides (Fe_4O_5, Fe_5O_6) are among the most prominent representatives of the family of strongly correlated oxides, where the metal- insulator transition is accompanied by various changes in charge ordering; these structures have been studied using X-ray and neutron diffraction and X-ray scattering methods [7–9], Mössbauer spectroscopy and theoretically using the LSDA+U method [10,11]. First-principles approaches for the treatment of strong electronic correlations, such as the local density approximation with U correction (LDA+U) [12-14], LDA with dynamical mean-field theory (LDA+DMFT in LMTO-orbitals or plane waves [15, 16], Hartree–Fock methods with embedded clusters [17–20], differ significantly in their accuracy and resource efficiency.

Oxide films $(Fe_{1-x}Cr_x)_{3-d}O_4$ are of great importance for the corrosion resistance of steels in contact with lead coolant (a possible technological solution in fourth-generation nuclear reactors) [21,22]. During corrosion of ferritic/martensitic steels, the protective oxide film typically consists of an outer magnetite layer (Fe_3O_4) and an inner spinel layer $(Fe_{1-x}Cr_x)_{3-d}O_4$ [21, 22, 23, 24], where $x = 0.20 - 0.23$ [25]. It is assumed that the growth of the inner chromium-containing layer occurs towards the steel and is primarily regulated by oxygen diffusion from the coolant inward, while the outer magnetite layer grows outward due to iron diffusion in the opposite direction; chromium diffusion from the steel is limited [22–25]. Understanding the predominant mass transfer mechanisms in the corrosion kinetics of protective oxide films requires knowledge about the content and transport of point defects in these oxides [26].

Density functional theory (DFT) calculations demonstrate the detrimental effect of lead and bismuth on the corrosion resistance of oxide films [27–29], while the presence of oxygen on the steel surface at a certain concentration indeed prevents unlimited corrosion [30]. However, within the framework of the mentioned corrosion models, very few first-principles calculations are devoted to the thermodynamics of point defect formation in oxides $Fe(Fe_{1-\ x}Cr_x)_2O_4$ ((see below).

The spinel structure corresponds to the general formula AB_2O_4, where A is the cation sublattice site with tetrahedral, and B with octahedral oxygen coordination (Fig. 1). Magnetite $Fe_{3-\ d}O_4$, a prominent representative of the strongly correlated transition metal oxides family, is an inverse spinel $A^{3+}B1^{2+}B2^{3+}O_4$ of space group $Fd\bar{3}m$. under normal conditions. Iron atoms in octahedral sites (B-sites) have an average oxidation state of +2.5, while atoms in tetrahedral sites (A-sites) have an oxidation state of +3 and magnetic moments ordered antiferromagnetically to the moments at B-sites (thus, magnetite is a ferrimagnet with a Neel temperature of about 860 K). An abrupt drop in electrical conductivity and symmetry lowering to monoclinic is observed below $Tv \simeq 120$ K (Verwey transition) [31–33]. Chromite $FeCr_2O_4$, in comparison, is a normal spinel $A^{2+}B_2^{3+}O_4$, also with mutual antiferromagnetic ordering of A and B sublattices, and has at least two characteristic transitions besides the ferrimagnet-paramagnet transition. One is associated with the cooperative Jahn–Teller effect (JT) and crystal symmetry lowering system to tetragonal due to the presence of JT-active ions Fe_A^{2+}, occurring at $T_{JT} \simeq 135$ K [34–36]. The second is related to dynamic spin frustration in the B sublattice (which persists despite JT symmetry lowering), leading to conical spin structures below $T_c \simeq 35$ K and significantly lowering the Neel temperature to approximately 80 K compared to Fe_3O_4 [34, 35, 37, 38].

This work analyzes the electronic structure of defect-free cubic phases of magnetite and chromite. Then, a brief review of the experimental research cycle by Dieckmann and co-authors on the study of point defects in magnetite at high temperatures is presented. Further, the theoretical and computational methods within the DFT+U approximation used in the work are described, along with the thermodynamic analysis of magnetite and chromite stability, necessary for determining the conditions under which defect formation energies will be analyzed. The description of calculation results is followed by their discussion in the context of available experimental data.

2. ELECTRONIC PROPERTIES OF MAGNETITE AND CHROMIUM SPINELS

2.1. Charge ordering in Fe_3O_4

Many theoretical studies have been devoted to the Verwey transition mechanism and first- principles calculations of the ground state electronic structure of magnetite in the low- temperature (LT) phase [39-44]. The results of these works agree that the LT phase possesses long-range charge ordering of Fe_B^{2+} and Fe_B^{3+} atoms and orbital ordering of $t_{2g,}$–-orbitals Fe_B^{2+} (short-range orbital order is noted in accordance with the Kugel-Khomskii model [1, 40, 44]). This disproves the mechanism proposed by Verwey, which was attributed to the emergence of so-called Verwey short-range charge ordering of Fe_B-atoms, intended to minimize the energy of electrostatic interaction between electrons [45]. However, as correctly noted in [46], two different views on the primary cause of the transition can be traced in the mentioned works. Namely, the authors of [39] emphasized charge ordering and electron-electron interaction, while in [41] the purely electronic mechanism of charge ordering stabilization is refuted in favor of JT distortions. Works [42,43] noted the decisive role of electron-phonon interaction of a more complex nature than ordinary JT interaction, and primarily the phonon X_3-mode in the emergence of the band gap and symmetry reduction in the low-temperature phase of magnetite.

The state-of-the-art model [47-49] suggests that the excess electron is localized as a small polaron, but not at a single site Fe_B^{2+}, but at three adjacent sites at once: to describe such disproportionation of atoms Fe_B^{2+} and Fe_B^{3+} (and their associated displacements), quasiparticles called trimerons have been proposed, which are detected in the LT-phase of magnetite through X-ray structural analysis [47,48] and theoretically [49]. The emerging trimeron charge ordering and polaronic JT effect on Fe_B^{2+}-atoms are elements of a common mechanism

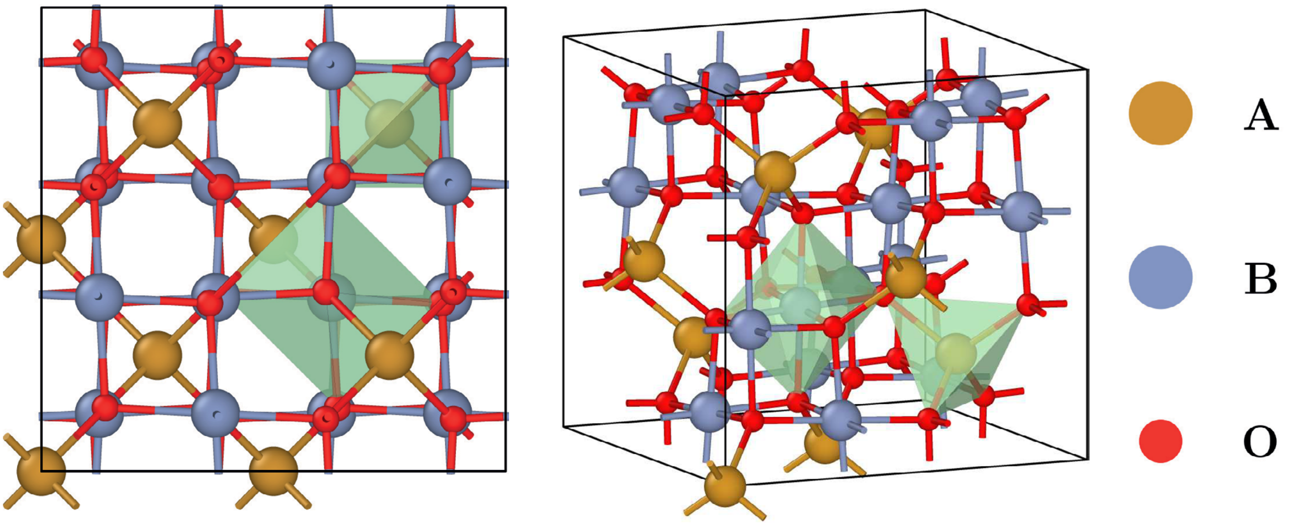

Fig. 1. Cubic unit cell of spinel AB_2O_4 space group $Fd\bar{3}m$ (56 atoms). Tetrahedral and octahedral oxygen environments are shown in green

of the Verwey transition [46]. More specifically, the charge ordering, present within the short-range but not fully understood order at $T > T_V$ and the long-range trimeron ordering at $T < T_V$, modulates the X_3-mode due to its particularly strong electron-phonon coupling [50, 51]. Thus, the Verwey transition has a mixed nature, determined by both electronic and lattice degrees of freedom [50].

The DFT+U method, being highly effective in describing strongly correlated systems [12-14], can reproduce the splitting of the $t_{2g,}$-(B)- (B)-electron peak and, consequently, the emergence of a band gap and charge disproportionation in B-sites of the LT-phase [10, 39, 40, 42]. For a long time, it was believed that at $T > T_V$, i.e., in the cubic high-temperature (HT) phase, magnetite was a half-metal [39, 41, 42, 52]. Nevertheless, many experiments prove that with increasing temperature, the band gap E_g remains finite and only narrows significantly by more than 50 meV. This is reflected in the results of photoemission spectroscopy ($E_g(HT) \simeq 100$ meV, $E_g(LT) \simeq 150$ meV, [53, 54]), optical conductivity spectroscopy (0.14 eV [55]), scanning tunneling spectroscopy on nanocrystals ($E_g(HT) \simeq 75 \pm 10$ meV, $E_g(LT) \simeq 140–320$ meV [56, 57]). Calculations using the LDA + DMFT method also showed [58] that the band gap width is $E_g \simeq 0.051$ meV in the HT-phase and $E_g \simeq 0.087$ meV in the LT-phase. However, the authors arrived at a somewhat narrower band gap in the LT-phase and, according to current understanding, incorrect, conclusions about the predominant role of JT-distortions in the Verwey transition mechanism, underestimating the importance of charge ordering. The structural distortions themselves were considered indirectly, only through self-consistent variation of the parameter D splitting of t_{2g}(B)-orbitals until the destabilization of the HT- spectrum relative to the LT-spectrum at D = D_c. Furthermore, in work [58], the parameters U and J DMFT-of the DMFT Hamiltonian were taken from works [10] and [40], but the value V = 0.4 eV used in this Hamiltonian for the Coulomb interaction parameter between different sites differed from the value of 0.18 eV in work [10]. The presence of short-range charge ordering in Fe_B-sites at $T > T_V$ was later confirmed by X-ray scattering methods [7,46]; it also indirectly follows from the energy differences in DFT calculations [59] and entropy change [45,53] between monoclinic and cubic phases and some peculiarities of behavior of experimental and theoretical phonon spectra [50]. This excludes (at least in some range of $T > T_V$) the correctness of ideas about the delocalization of $t_{2g,}$-(B)-electron within $Fd\bar{3}m$ symmetry and about identical oxidation states $Fe_B(+2.5)$. Some calculations of the $Fd\bar{3}m$-phase of magnetite within DFT+U models or hybrid DFT reproduce the band gap in the minor (spin “down”) component of the density of electronic states (DOS) precisely due to this symmetry lowering of the electronic wave function, but not the crystal structure [60–62].

Among the most recent examples of Fe_3O_4 modelling, works [59, 63, 64] should be mentioned. The authors of [59] conducted detailed calculations using the method and studied the influence of local Fe-environment on the formation energies of neutral and charged oxygen vacancies in the low-temperature phase of magnetite, and also found numerical confirmation of short-range order in the HT-phase. In work [63], the DFT+U+V method was used to describe the ground state in the cubic phase, however, an incorrect half-metallic DOS distribution was obtained, while the results of the DFT+U calculations correctly reproduced the main DOS features and the presence of an isolated peak of Fe_B t_{2g}--iron electrons in the minor spin component, however, the valence band ceiling erroneously fell at the middle of this peak rather than at its upper boundary. Finally, calculations within classical molecular dynamics with ClayFF potential and Monte Carlo method [64] were able to describe the distribution and evolution of various oxidation states of B-iron atoms, while accounting for this disproportionation itself is a "bottleneck" in the problem of creating classical potentials for magnetite [65].

2.2 Chromium Spinels

Iron-chromium mixed composite spinels $Fe_{1+x}Cr_{2-x}O_4, 0 < x < 2$, and their thin films have been quite extensively studied in experiments [66–71]. Structural and magnetic phase transitions are reflected in phase $T-x$-diagrams. The presence of Fe_A^{2+} ions at $x < 2$ leads to the emergence of cooperative JT-effect (in chromite $T_{JT} \simeq 135$ K) with symmetry lowering [34–36, 67, 68, 70]. Moreover, magnetic frustration in the pyrochlore B-sublattice $Fe(Cr_B^{3+})_2O_4$ [37, 38] (and generally at $x < 0.6$ [70]) leads to conical spin structures and, consequently, a notable decrease in the Néel temperature to 80 K with decrease in x down to 0 in chromite $FeCr_2O_4$ [34, 35, 38, 66, 70]. The influence of x on exchange constants, critical temperature, charge distribution and polaronic transport in spinels $Fe_{1+x}Cr_{2-x}O_4$ and their thin films is thoroughly described in works [66,69,71]. In particular, it is noted that increasing the Cr fraction leads to decreased conductivity due to possible blocking of polaronic transfer along $Fe_B^{3+}-Fe_B^{2+}$ chains, since Cr^{3+} is most stable in these spinels, apparently due to the highest crystal field stabilization energy in octahedral coordination.

First-principles calculations of iron-chromium spinels are relatively rare and generally concern structures $FeCr_2O_4$ (chromite) [38, 72–75], $CrFe_2O_4$ [76, 77], as well as interfaces or solid solutions $Fe_3O_4-FeCr_2O_4$ [78, 79]. Chromite at room temperature is a normal spinel $(Fe_A^{2+}(Cr_B^{3+})_2O_4)$, however, the Néel temperature of 80 K, below which chromite exhibits ferrimagnetic ordering down to 35 K [35], is significantly below room temperature. In some theoretical works, the DOS of chromite appears characteristic of a half-metal [38, 72, 77, 79], but amounts to about 2 eV in GGA+U calculations [73–75, 78], see Table 1 (GGA - generalized gradient approximation). Meanwhile, the optical band gap of chromite is also finite $E_g = 1.3 - 1.5$ eV [38, 80, 81]. Note that in work [75], the value $E_g = 1.61$ eV is closest to experimental values (see Table 1). This can be explained by a more accurate selection of U parameters and the fact that relaxation of atomic coordinates in $Fd\bar{3}m$-phase was not carried out, and as a result, a better approximation to the cubic HT-phase was achieved.

Table 1. Band gap $FeCr_2O_4$, calculated in the GGA+U approximation

E_g, eV	U, eV	Year, source
2.09	3.7 (Fe), 3.2 (Cr)	2013 [78]
1.8	5.0 (Fe), 3.0 (Cr)	2015 [73]
2.15	4.3 (Fe), 4.0 (Cr)	2021 [74]
1.61	3.8 (Fe), 2.0 (Cr)	2023 [75]

Note. * Without relaxation of atomic coordinates in $Fd\bar{3}m$-structure

3. FORMATION AND MIGRATION ENERGIES OF POINT DEFECTS IN ACCORDING TO THE EXPERIMENTS OF DIECKMANN ET AL.

Point defects, which inevitably occur in any real crystals, have strong influence on their properties [82]. During the last decades of the previous century, Dieckmann et al. extensively studied the thermodynamics and transport of defects in non-stoichiometric oxides [83], particularly in magnetite [84–91] and derivative spinels [92–94]. One of the main problems, as indicated by the authors of [83], was the difficulty in interpreting experimental data from the perspective of ionic transport mechanisms in spinels due to the lack of clear understanding of defect-involved processes at the microscopic level at that time. A series of works by Dieckmann et al. on magnetite research brought much clarity to this issue.

In works [84-86], the authors measured residual radioactivity of isotopes Fe-59 during diffusion from the surface into the bulk of samples. Thus, in work [84], they measured the dependence of diffusion coefficients D^*_{Fe} of tracer elements at 900–1400 °C on partial oxygen pressure, showing characteristic V-shaped form in double logarithmic scale (Fig. 2). Based on the law of mass action, two regions were identified (high and low partial oxygen pressures) assuming that vacancy mechanism dominates in the former, and interstitial mechanism in the latter one. At each temperature, the obtained V-shaped dependence was described by formula [84, 89]

$$D^*_{Fe}(T,a_{O_2}) = D^\circ_V(T)\frac{a_{O_2}^{2/3}}{1+2K_V a_{O_2}^{2/3}} + D^\circ_I(T)a_{O_2}^{-2/3}, \qquad (1)$$

where D°_V and D°_I are partial diffusion coefficients for vacancies (V) and interstitials (I), $a_{O_2} = p_{O_2}/1$ andm is normalized oxygen activity, K_V is an equilibrium constant dependent on temperature. To extract true activation energies of defect diffusion from fictitious activation energies

$$E^\alpha_{fict} = -\frac{d\ln D^\circ_\alpha}{d(1/T)}, \alpha = V, I \qquad (2)$$

(to shed light on cation diffusion mechanisms), knowledge of formation energies of corresponding point defects is required. Dieckmann et al. proposed a point defect model for the cation sublattice of magnetite [85]. Thus, using the known temperature dependence of the equilibrium constant K_2 for iron vacancy formation reaction

$$3Fe^{2+}_{Fe} + \frac{2}{3}O_{2(g)} \overset{K_2}{\rightleftharpoons} 2Fe^{3+}_{Fe} + V_{Fe} + \frac{1}{3}Fe_3O_{4(g)} \qquad (3)$$

(index "(g)" indicates gas phase) the value $E^V_{act} = 137$ kJ/mol was obtained for the energy in the case of vacancy mechanism of iron diffusion from expression

$$E^V_{act} = -\left(\frac{d(\ln D^\circ_V - \ln K_2)}{d(1/T)}\right) = E^V_{fict} - E^V_{form}.$$

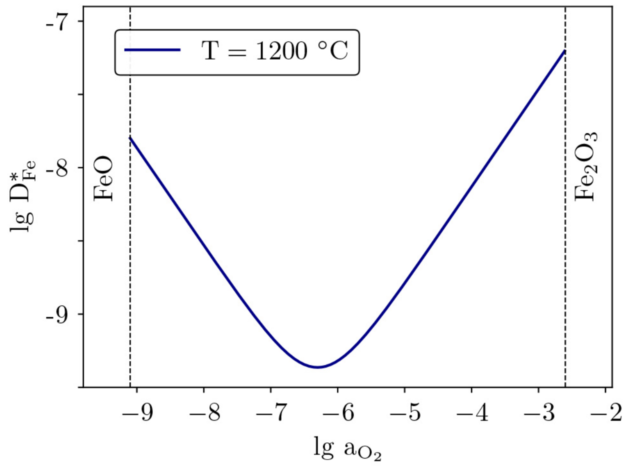

Fig. 2. Dependence of diffusion coefficient Fe-59 in magnetite on partial oxygen pressure at 1200 °C according to formula (1). The boundaries of magnetite-hematite (Fe_2O_3) and magnetite-wustite (FeO) buffers are indicated (according to work [84])

Since these data concerned only the range of high oxygen activities (vacancy mechanism), only constant K_2 and its temperature dependence could be known. For this reason, the activation energy for interstitial diffusion mechanism, connected with vacancy mechanism through Frenkel equilibrium,

$$\varnothing \overset{K_{FP}}{\rightleftharpoons} Fe_I^{z+} + V_{Fe} \qquad (4)$$

($\varnothing$—defect-free crystal) could not be obtained using only constant K_2, since value

$$-\left(\frac{d(\ln D^\circ_I + \ln K_2)}{d(1/T)}\right) = E^I_{act} - \frac{d(\ln K_5)}{d(1/T)} =$$

$$= E^I_{act} + E^{FP}_{form} = 330 \text{ kJ/mol}$$

included the formation energy of E^{FP}_{form} Frenkel pair Fe_I / V_{Fe} [86]. unknown to the authors at that time.

In order to obtain their own data on the defect concentration across the entire stability range of magnetite at 900–1400 °C, Dieckmann et al. used thermogravimetric analysis in works [87, 89]. The authors arrived at the following relationship for used thermogravimetric the deviation from stoichiometry δ in $Fe_{3-\delta}O_4$ (essentially, a titrimetric curve) [87]:

$$\delta = \sum_i [V_{Fe}] - \sum_{i,z} [Fe_I^{z+}] =$$

$$= \frac{K_V(T)}{4}\frac{a_{O_2}^{2/3}}{1+2K_V(T)a_{O_2}^{2/3}} - 4K_I(T)a_{O_2}^{-2/3} \qquad (5)$$

(summation is performed over possible charge states z and inequivalent configurations i). From the titration curves, Arrhenius temperature dependencies of constants K_V and K_I were obtained with activation energies of –226 kJ/mol for K_V and 358 and 526 kJ/mol for $K_{I'}$ and $K_{I''}$ respectively [89] (the behavior of K_I could not be described within a single exponent by the authors of work [89], therefore $K_I = K_{I'} + K_{I''}$). The true activation energies of diffusion (migration barriers) of point defects, calculated [91] without specifying migration mechanisms in the form of

$$E_{act}^{V} = -\left(\frac{d(\ln D_V^{\circ} - \ln K_V)}{d(1/T)}\right),$$

$$E_{act}^{I} = -\left(\frac{d(\ln D_I^{\circ} - \ln K_I)}{d(1/T)}\right),$$

were 0.9 eV for vacancies and 2.65 eV for interstitials. For fictitious activation energies for partial coefficients D_V°, D_I° according to formula (2) from [84], values of –139 and 614 kJ/mol were obtained respectively [89, 91].

In the work [89], thermogravimetry was used to monitor the sample mass over time during the relaxation of defect concentration profiles after a sharp change in p_{O_2}. Based on the measured time dependencies, the authors calculated the chemical (ionic) diffusion coefficient D_{ion}, directly related to the diffusion coefficients and concentrations of point defects by equation $D_{ion}c_{ion} = \sum_{def} D_{def}c_{def}$ (c_{ion} — effective concentration of ions participating in diffusion). Following the logic of previous works, the authors identified regions with predominantly vacancy or interstitial diffusion mechanisms and introduced coefficients D_V, D_I instead of a single D_{ion}. Thus, the authors supplemented the observation of Fe diffusion in space using the tracer method [84] with complementary temporal analysis [89] and established their formula connection through equilibrium constants from [87], namely

$$D_V = \frac{12D_V^{\circ}}{K_V f_V}, D_I = \frac{3D_I^{\circ}}{4K_I f_I}, \tag{6}$$

where f_V and f_I are average correlation factors for vacancy and interstitial diffusion in the random walk model. Introducing the temperature dependence of factor f_V,

$$f_V = \frac{0.5\eta_{tet}D_{V(tet)} + 0.56(1-\eta_{tet})D_{V(oct)}}{\eta_{tet}D_{V(tet)} + (1-\eta_{tet})D_{V(oct)}}, \tag{7}$$

from the consideration that the fraction of vacancies in tetrahedral (A) sites changes as

$$\eta_{tet} = \frac{1}{1 + a\exp\{(b/T)\}},$$

and the diffusion coefficient equals

$$D_V = \eta_{tet}D_{V(tet)} + (1-\eta_{tet})D_{V(oct)}$$

(0.5 and 0.56 are correlation factors for A- and B-vacancy diffusion respectively [95], a, b are some fitting parameters), the authors used the temperature dependence of

$$\frac{12D_V^{\circ}}{K_V} = 0.5\eta_{tet}D_{V(tet)} + 0.56(1-\eta_{tet})D_{V(oct)}$$

to determine a and b activation energies for diffusion coefficients $D_{V(tet)}, D_{V(oct)}$ measured in [89] and calculated using formulas (6) and (7), and data from works [84, 87]. Thus, Dieckmann et al. managed to obtain some insights into vacancy diffusion at the micro level and distinguish between activation energies of 0.75 eV and 1.26 eV for octahedral and tetrahedral vacancies respectively [89]; the fraction of the latter increases with temperature. When considering only octahedral vacancies in (7) ($\eta_{tet} \approx 0, f_V \approx 0.56$) the previously indicated value of 0.9 eV was obtained. For the activation energy of interstitial diffusion, based on thermogravimetry results [89], a value of 2.37 eV was obtained. It is evident that both latter values are in good agreement with those mentioned in the previous paragraph (based on tracer diffusion measurements [84] and non-stoichiometry [87]). The mechanism of interstitial diffusion, however, remained unspecified. Table 2 summarizes the migration barrier data from Dieckmann et al.'s works.

The results of various experiments on the diffusion of oxygen and various transition metal cations in magnetite and derivative spinels are presented in review [96]. Thus, Cr racer atoms have the lowest diffusion coefficients in magnetite and mixed Fe–Cr-spinels (three orders of magnitude lower than Fe, atoms, see also [92]), however, the dependencies on O_2 partial pressure are identical. Defects in the anion sublattice are considered secondary [97], but the lack of diffusion coefficient measurements in both sublattices under the same external conditions (oxygen partial pressure) makes it difficult to compare their temperature dependencies.

Table 2. Activation energies for diffusion of cationic point defects in Fe_3O_4 (eV) from works [89, 91] (vac — vacancies, int — interstitials)

Method vac int	vac	int
Tracer method [84] + static thermogravimetry [87]	0,9* 1.26 (A) 0.75 (B)	3*2.37
Time-domain thermogravimetry [89]	0.9	2.65

Note. $^*fV \equiv fV(B) = 0.56$ in (7).

DFT and DFT+U approximations can provide sufficiently comprehensive information about thermodynamic and kinetic properties of point defects in magnetic iron oxides, such as hematite Fe_2O_3 [98], however, similar studies of magnetite, especially its HT-phase, are incomplete and fragmented. Thus, the authors of [99] studied the migration of octahedral vacancies in spinels $MeFe_2O_4$, Me=Fe, Co, Ni and obtained a migration barrier of 0.7 eV for B-vacancy in Fe_3O_4 in agreement with Dieckmann et al. [89], but used incorrect magnetic ordering in magnetite. The first consistent approach to modeling point defects in the cubic phase of magnetite using the method, based on the semiconducting ground state with Verwey ordering, is described in works [61, 62], but concerns only the cation sublattice. In the detailed study of oxygen vacancies [59], considerable attention was also paid to charge ordering. The present work covers the most complete set of possible point defects in magnetite and chromite, however, migration barrier calculations were not performed.

4. THEORETICAL AND COMPUTATIONAL METHODS

With careful selection of the parameter *U* for better description of properties of a specific iron oxide, the DFT+U method is capable of describing electronic and thermodynamic properties of the crystal at an accuracy level almost matching that of DFT with hybrid density functionals [100]. Moreover, hybrid functionals like HSE themselves contain uncertainty in choosing the screening parameter and, as in the case with *U* in the DFT+U method, when decreasing this parameter, they can also lead to the disappearance of the band gap in the minor DOS component of magnetite [60,100]. Since uniform studies of point defects in spinels $Fe_{1+x}Cr_{2-x}O_4$ from first principles are absent, in this work, using the DFT+U method, calculations of formation energies of neutral point defects were performed in both cation and oxygen sublattices of magnetite and chromite for two boundary cases at x=2,0. Point defect formation energies depend on chemical potentials of elementary components, therefore, first of all, from stability conditions of Fe_3O_4 and $FeCr_2O_4$ and using Gibbs formation energies of various Fe and Cr oxides from the thermochemical database [101], the limits of variation of these values were found in good agreement with experimental stability boundaries. Since it is the high-temperature cubic $Fd\bar{3}m$-phases of Fe_3O_4 and $FeCr_2O_4$ that were investigated, special attention in our work was paid to the correct approximation to the ground state of the electronic subsystem to minimize low-temperature DFT artifacts. Finally, defect configurations with lowest energy were described and point defect formation energies were calculated considering only the contribution from electronic and ionic system optimization, neglecting volume effects and contributions from phonon and electronic entropies. The results obtained in our work show good quantitative agreement with other first-principles calculations of point defect formation energies in Fe_3O_4 and works by Dieckmann et al., which largely justifies our chosen approximations and reliability of results obtained for $FeCr_2O_4$.

The calculations were performed using the VASP software package [102-104]. The projector augmented waves (PAW) method [105] was used to approximate the electron density near atomic nuclei in combination with the generalized gradient approximation for the exchange- correlation potential at the level of Perdew-Burke-Ernzerhof functional (PBE GGA) [106]

PAW pseudopotentials Fe($4s2\,3d6$), Cr($4s1\,3d5$) and O($2s2\ 2p4$). were selected. 56-atom cubic cells were used in the calculations (see Fig. 1). The plane wave cutoff energy was 550 eV, resolution of Γ -centered k-grid — $4 \times 4 \times 4$, convergence criteria for self-consistent cycles were $10^{-6}(10^{-5})$eV for electronic (ionic) steps. No symmetry constraints were imposed on the electron density, as this is fundamentally important for the disproportionation of +2 and +3 charge states between octahedral iron sites in magnetite [60-62]. The tetrahedron method [107] was used to approximate the electronic distribution function when integrating in the first Brillouin zone. Although the reference literature data we mention concern temperatures for magnetite (and especially $T > T_N \simeq 860$ K for magnetite (and especially $T > T_N \simeq 80$ K for chromite), spin polarization with collinear magnetic moments was included in all calculations. To account for strong electronic correlations, the DFT+U approach in Dudarev's modification [108] with $U_{\text{Fe}} = 3.5$ eV [60, 61, 62], $U_{\text{Cr}} = 2.0$ eV [75]. was used. Optimal parallelization strategies in VASP computations in VASP were applied [109].

OVITO software [110] was used for structure visualization. The pymatgen package [111] was used for output file processing, and the ShakeNBreak package [112, 113] was used to ensure more “meticulous” relaxation in defect structures.

The energies (enthalpies) of formation of neutral defects were calculated using the formula

$$E_{form} = E_{def} - E_0 - \Delta n_i \mu_i \tag{8}$$

where E_{def} is the energy of the defective supercell in DFT+U, E_0 is the energy of the defect- free supercell inDFT+U, $\Delta n_i = \pm 1$ depending on the defect type (a vacancy or an interstitial), $\mu_i = \mu_i^0 + \Delta\mu_i$ is the chemical potential of an added or removed atom. In the case of $FeCr_2O_4$ additional calculations of formation energies for the most favorable configurations of vacancies and interstitials were performed on the 6 × 6 × 6 grid, but the relative changes in $E_{def} - E_0$ values were less than 1%. The choice of reference chemical potentials μ_i^0 is not restricted, however: 1) they must be referenced to the same thermodynamic parameters (T, P) for all the elements in the composition of the considered phase; 2) although the absolute values of μ_i^0 have no meaning, like the energies of supercells in DFT+U, all these values must be calculated within the same approximation. The negative addition $\Delta\mu_i$ varies within the thermodynamic stability limits of the phase (see section 5). For oxygen $O_{2(g)}$ this correction can be related to its partial pressure in the ideal gas approximation ($\Delta\mu_i = \Delta\mu_i(P), P = p_{O_2}$):

$$\begin{aligned}\mu_{i.g.}(T,P) &= G^{DFT}_{i.g.}(T_0,P_0) + \\ &+ (H(T,P_0) - H(T_0,P_0)) - \\ &- (TS(T,P_0) - T_0S(T_0,P_0)) + T\ln\left(P / P_0\right) = \\ &= \mu^0_{i.g.}(T,P_0) + T\ln\left(P / P_0\right),\end{aligned} \tag{9}$$

where G is the Gibbs energy, H is enthalpy, S is entropy, the index "DFT“ means that the value $G_{i.g.}(T_0,P_0)$ must be calculated within the framework of the approximation used in the work. In our case, since the triplet of molecular oxygen is incorrectly described in GGA, in the first term we could not set $T_0 = 0, P_0 = 0$. Therefore, we set $T_0 = 298.15\,\text{K}$ and $P_0 = 1\,atm$ and found

$$G^{DFT}_{O_2(g)}(T_0,P_0) = -9.74\,eV$$

based on 1) our calculated DFT energies $H^{DFT}_{H_2,H_2O(g)}(T = 0, P = 0)$ of molecules H_2 and H_2O, converted to Gibbs energies $G^{DFT}_{H_2,H_2O(g)}(T_0,P_0)$ using thermochemical data [101]; 2) Gibbs energy $\Delta Gc(T_0,\ P_0) = -4.92$ eV/O_2 for the hydrogen combustion reaction under normal conditions, after which we obtained

$$\begin{aligned}G^{DFT}_{O_2(g)}(T_0,P_0) &= 2(G^{DFT}_{H_2O(g)}(T_0,P_0) - \\ &- G^{DFT}_{H_2(g)}(T_0,P_0)) - \Delta G^c(T_0,P_0).\end{aligned}$$

The second and third terms in (9) for recalculating $G^{DFT}_{O_2(g)}(T_0,P_0)$ from $T = T_0$ to the required temperaturee $T = 1500$ K (this temperature was chosen since most of the relevant experimental data are closest to it) according to formula (9) were also taken from the database [101]. In total, the first three terms in (9) at $T = 1500$ K gave the value

$$\mu^0_{O_2(g)}(T,P_0) = -6.357\,ev / O.$$

The last term in (9) is the additive $\Delta\mu_{O_2(g)}(P)$.

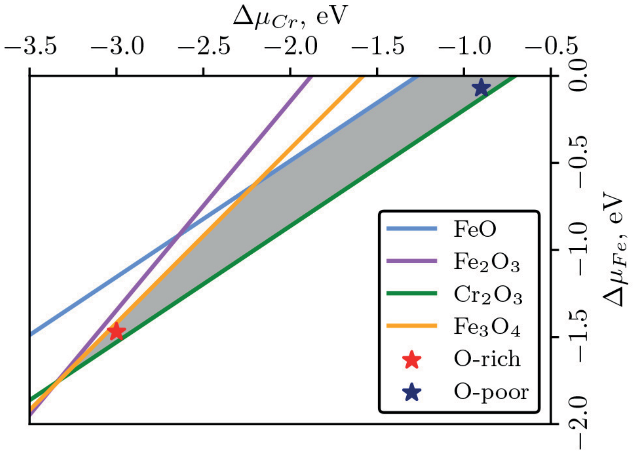

Fig. 3. Phase stability diagram $\mathrm{FeCr_2O_4}$. The gray-filled area shows where $\mathrm{FeCr_2O_4}$ is stable and competing oxides are unstable. Red and blue markers indicate representative points for conditions of excess ($\Delta\mu_{\mathrm{O}} = -0.59$ eV in B) and deficiency ($\Delta\mu_{\mathrm{O}} = -1.99$ eV in B) oxygen respectively

The chemical potentials of Fe and Cr were also calculated as Fe and Cr were also calculated as $\mathrm{m}_i^0 + \mathrm{Dm}_i$, where m_i^0 is the energy of the elementary BCC phase of metal per atom in DFT+U ($\mathrm{m}_{\mathrm{Cr}}^0 = -7.774$ eV/atom, $\mathrm{m}_{\mathrm{Fe}}^0 = -5.571$ eV/atom), Dm_i is the negative additive due to the difference between the considered phase and pure metal. The next section is devoted to calculating the limits of change Dm_i.

5. THERMODYNAMIC STABILITY BOUNDARIES FOR CHEMICAL POTENTIALS

Additional chemical potentials Dm_i of elementary components in the region of thermodynamic stability $\mathrm{Fe_3O_4}$ or $\mathrm{FeCr_2O_4}$ are related by the following equations respectively

$$\begin{aligned} &3\mathrm{Dm}_{\mathrm{Fe}} + 4\mathrm{Dm}_{\mathrm{O}} = \mathrm{D}G_{form}(\mathrm{Fe_3O_4}), \\ &\mathrm{Dm}_{\mathrm{Fe}} + 2\mathrm{Dm}_{\mathrm{Cr}} + 4\mathrm{Dm}_{\mathrm{O}} = \mathrm{D}G_{form}(\mathrm{FeCr_2O_4}), \end{aligned} \tag{10}$$

where $\mathrm{D}G_{form}$ are the Gibbs energies of phase formation, while for competing phases $\mathrm{Fe}_x\mathrm{Cr}_y\mathrm{O}_z$ the following inequalities must hold

$$x\mathrm{Dm}_{\mathrm{Fe}} + y\mathrm{Dm}_{\mathrm{Cr}} + z\mathrm{Dm}_{\mathrm{O}} < \mathrm{D}G_{form}(\mathrm{Fe}_x\mathrm{Cr}_y\mathrm{O}_z), \tag{11}$$

indicating their instability relative to the phases of elementary components (competing phases are $\mathrm{Fe_2O_3}$ ans FeO, as well as additionally $\mathrm{Cr_2O_3}$ and $\mathrm{CrO_2}$ for chromite). The Gibbs energies of phase formation $\mathrm{D}G_{form}$ in this work were taken from the NIST database [101] for $T = 1500$ K. Thus, for magnetite

$$\begin{aligned} &3\mathrm{D}G_{form}(\mathrm{Fe_2O_3}) - 2\mathrm{D}\ G_{form}(\mathrm{Fe_3O_4}) > \mathrm{Dm}_{\mathrm{O}} > \\ &> \mathrm{D}G_{form}(\mathrm{Fe_3O_4}) \qquad - 3\mathrm{D}G_{form}(\mathrm{FeO}). \end{aligned} \tag{12}$$

After recalculation according to the formula

$$\mathrm{Dm}_{\mathrm{O}} = \frac{1}{2}T\ln\left(\frac{P}{P_0}\right)$$

the sought stability boundaries were

$$-8.06 < \lg p_{\mathrm{O}_2} < -2.23$$

in good agreement with the values of -8.9 and -2.4 пobtained by Dieckmann et al., see Fig. 7 in work [87].

Similar correlations were made in the case of chromite $\mathrm{FeCr_2O_4}$, whose formation energy relative to was absent in the NIST JANAF tables and was calculated using data from work [114] (» - 945 kJ/mol). The stability diagram in Fig. 3 accurately reproduces the lower boundary (oxygen deficiency), $\lg(p_{\mathrm{O}_2}^{poor} / P_0) = -14.15$ compared to values of -14.37 at 1473 K [115], -14 at 1473 K [92], -13.7 at 1500 K [116]. However, the upper boundary $\lg(p_{\mathrm{O}_2}^{rich} / P_0) = -2.41$ relatively well reproduces the result of -5.20 from work [115], but is significantly overestimated compared to values of -12.5 [92] and -11.7 [116]. from work [115], but is significantly overestimated compared to values of $(\mathrm{Fe}_{1-x}\mathrm{Cr}_x)_3\mathrm{O}_4$ on phase diagrams $p_{\mathrm{O}_2} - x$ [92, 116], experiences a very steep decline towards the lower boundary when approaching x ® $2/3$ (as if $\mathrm{FeCr_2O_4}$ composition corresponded to a single allowed oxygen pressure), which may lead to large errors in determining this boundary.

6. RESULTS

6.1 $\mathrm{FeMe_2O_4}$ (Me = Fe, Cr): ground state model of the cubic phase

To describe the defect-free cubic phase of magnetite and chromite using the DFT method, as emphasized in works [62, 75], not only the cell shape but the atomic positions were kept unrelaxed, maintaining the lattice belonging to the space group $Fd\bar{3}m$ (Wyckoff positions $8a$, $16c$, $32e$, for A-,

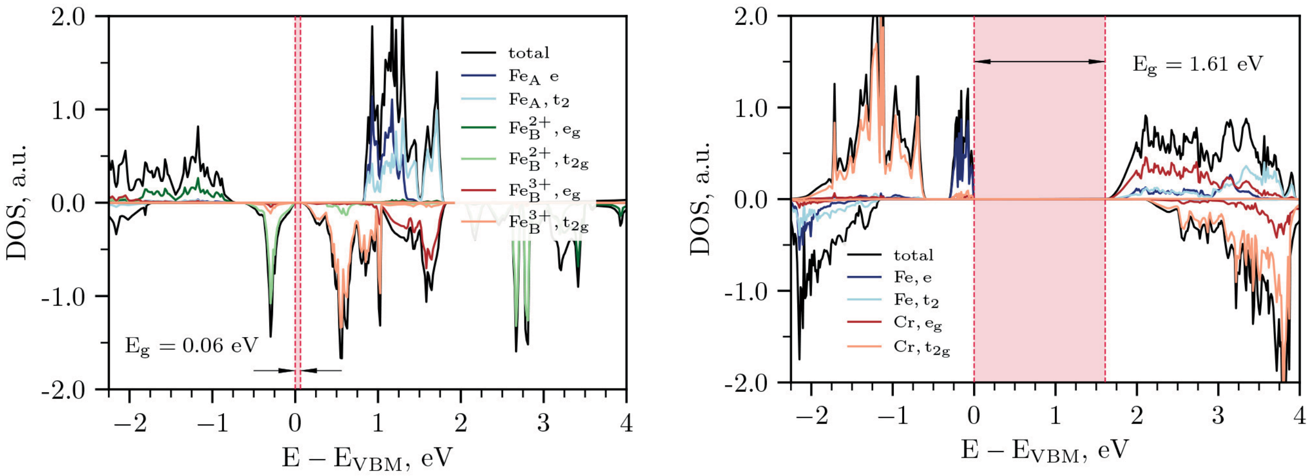

Fig. 4. Density of electronic states (DOS) Fe_3O_4 (left) and $FeCr_2O_4$ (right). The valence band maximum (VBM) is set to 0. The band gap *Eg* is shown in pink

B- and oxygen sublattices, oxygen atom displacement $u = 0.0049$ в Fe_3O_4 in $u = 0.0126$ in $FeCr_2O_4$), Only the lattice parameter was optimized. However, lowering of electronic density symmetry was allowed. Balancing again between the need to remain within static calculations at 0 K using DFT method and the desire to approximate the HT-phase, where charge ordering is short-range and can eventually disappear, we achieved charge disproportionation in the B-sublattice of magnetite in accordance with Verwey ordering in the ground state [61]. The lattice parameter minimizing energy was 8.474 Å for Fe_3O_4 and 8.488 Å for $FeCr_2O_4$ and was fixed in subsequent calculations.

Fig. 4 on the left shows the orbitally-resolved DOS of cubic magnetite. Notably, there is a narrow but finite band gap of $E_g = 0.06$ eV. As in the monoclinic LT-phase [40], the band gap relates to the splitting of t_{2g}-orbitals of atoms Fe_B^{2+} and Fe_B^{3+} due to charge ordering. The narrow t_{2g} - ïèê peak in the minor DOS component at the valence band maximum corresponds to an electron localized on atom Fe_B^{2+} The DOS of chromite $FeCr_2O_4$ is shown in Fig. 4 on the right, with a band gap of 1.61 eV, and the valence band maximum corresponds to the *e* - ïèê peak of the extra electron on atom Fe_A^{2+}. The main characteristics of the two spinels in the ground state are summarized in Table 3.

Based on the occupancy matrices obtained as a result of the method, it can be concluded that metal ions correspond to high-spin configurations $Fe_B^{3+}\, t^3_{2g,-}e^2_{g,-}$, $Fe_B^{2+}\, t^3_{2g,-}e^2_{g,-}t^1_{2g,}-$, $Fe_A^{3+}\, e^2_- t^3_{2,}-$ in Fe_3O_4 and $Cr_B^{3+}\, t^3_{2g,-}e^0_{g,-}$, $Fe_A^{2+}\, e^2_- t^3_{2,}-e^1_-$ in $FeCr_2O_4$. According to the eigenvalues of occupancy matrices rounded to integers, the moments of Fe^{3+}, Fe^{2+} and Cr^{3+} can be identified with 5, 4, 3 μ_B. The total moments of the cells were thus, $8 \cdot 5 + 8 \cdot 4 - 8 \cdot 5 = 32\ \mu_B$ in Fe_3O_4 and $16 \cdot 3 - 8 \cdot 4 = 16\ \mu_B$ in $FeCr_2O_4$.

Table 3. Lattice parameter *a*, magnetic moments of cations *m*, magnetic moment of the cell *M*, band gap E_g of the cubic $FeMe_2O_4$, Me = Fe, Cr

Me	*a*, Å	*m*,m$_B$	*M*,m$_B$	E_gýÂ
Fe	8.47	4.1 (Fe_B^{3+}), 3.7 (Fe_B^{2+}) - 4.0 (Fe_A^{3+})	32	0.06
Cr	8.49	2.9 (Cr_B^{3+}) - 3.7(Fe_A^{2+})	16	1.61

6.2 Formation Energies of Neutral Defects

The designations of interstitial positions in the cation sublattice of spinel (two tetrahedral A1, A2 and octahedral B) in our work are similar to those described in [62], but the list of studied point defects was expanded ($Fe_{A1,A2,B,int}$, $V_{Fe,A,B}$, $O_{A1,A2,B,int}$, V_O in Fe_3O_4 and $Fe_{A1,A2,B,int}$, $V_{Fe,A}$, $Cr_{A1,A2,B,int}$, $V_{Cr,B}$, $O_{A1,A2,B,int}$, V_O in $FeCr_2O_4$). In $FeCr_2O_4$ the antisite defect was additionally considered Fe–Cr. Furthermore, the ShakeNBreak method was used for a more complete coverage of the configurational space of each defect structure and to avoid the problem of local structural minima during relaxation. Finally, since the occupation matrices of *d*-orbitals and magnetic ordering in defect cells were *a priori* unknown, when modeling cation defects, the magnetic moments on metal atoms and the total cell moment at the beginning of calculation were initialized in different ways. In some cases, changes in spin ordering on one or two cations were also allowed. The measures we took, although only partially and indirectly, helped to overcome the more global problem of local minima in the DFT+U method as based on the orbital-dependent density functional [117, 118]

To calculate the formation energies using formula (8) the work used chemical potential values simulating conditions at the upper and lower stability boundaries of chromite on the partial pressure scale O_2 (markers in Fig. 3). Note that at the lower boundary, chromite can coexist with pure iron. In the case of magnetite, the lower boundary was chosen based on the same considerations $\lg p_{O_2}^{min} = - 8.06$,see Section 5), however, the upper boundary was taken as –2.23, rather than –4.76. This corresponds to the value of the upper stability boundary of magnetite$p_{O_2}^{max}(T)$ in contact with lead melt containing dissolved oxygen, which was found by extrapolating the dependence $\ln p_{O_2}^{max}(T)$ to 1500 K (see Fig. 6 in work [23]). Table 4 contains all chemical potential values used in the calculations.

The calculated defect formation energies in Fe_3O_4 and $FeCr_2O_4$ are grouped in Table 5. For clarity, the lowest values among O interstitials in both spinels and Fe and Cr interstitials in chromite were selected. Note that, in general, the formation energies are generally noticeably higher in $FeCr_2O_4$, than in Fe_3O_4. This may be related to the fact that iron ions in octahedral (B) sites of magnetite exhibit mixed valence, which enables effective screening of charge density changes caused by defect appearance through changing the ratio of di- and trivalent cations [87].

Table 4. Chemical potentials μ_i, selected for calculating point defect formation energies according to (8); numbers on the left correspond to O_2 deficiency conditions O_2, and to its excess – on the right

Me	m_{Fe}ýÂ	m_{Cr}ýÂ	m_OýÂ
Fe	(- 6.20 ├ 6.85)	(- | -)	(- 7.56 ├ 7.07)
Cr	(- 5.64 ├ 7.04)	(- 8.67 ├ 10.77)	(- 8.35 ├ 6.95)

Table 5. Formation energies of neutral point defects and Frenkel pairs Fe_I/V_{Fe}, Cr_I/V_{Cr}, O_I/V_O eV. The lowest values for each type of defect are shown*

Fe_3O_4	rich**	poor	$FeCr_2O_4$	rich	poor
Fe_{A1}-*int*	2.16	1.51	Fe–Cr***	1.74	1.74
Fe_{A2}-*int*	2.13	1.48	Fe-*int*	4.85	3.45
Fe_B-*int*	1.14	0.49	Cr-*int*	6.66	4.56
A-*vac*	1.19	1.84	Fe-*vac*	1.77	3.17
B-*vac*	0.07	0.72	Cr-*vac*	1.38	3.48
O-*int*	2.37	2.86	O-*int*	3.57	4.97
O-*vac*	0.53	0.04	O-*vac*	3.00	1.60
Fe_{Bint} / V_B	1.21		Cr_{int} / V_{Cr}	8.04	
Fe_{Aint} / V_A	3.32		Fe_{int} / V_{Fe}	6.62	
O_{int} / V_O	2.90		O_{int} / V_O	6.57	

Note.

*The lowest values in each column are highlighted in bold.

**rich/poor – conditions of excess/deficiency O_2.

***Antisite defect Fe – Cr.

6.2.1. Magnetite

According to [62] and our results, vacancies and interstitials in B-sites are among the most easily formed defects of the iron sublattice, however, it should be added that neutral oxygen vacancies also have low formation energies, unlike interstitials. Under oxygen-rich conditions, iron vacancies are most easily formed, which is expected within Dieckmann's point defect model [87], see expression

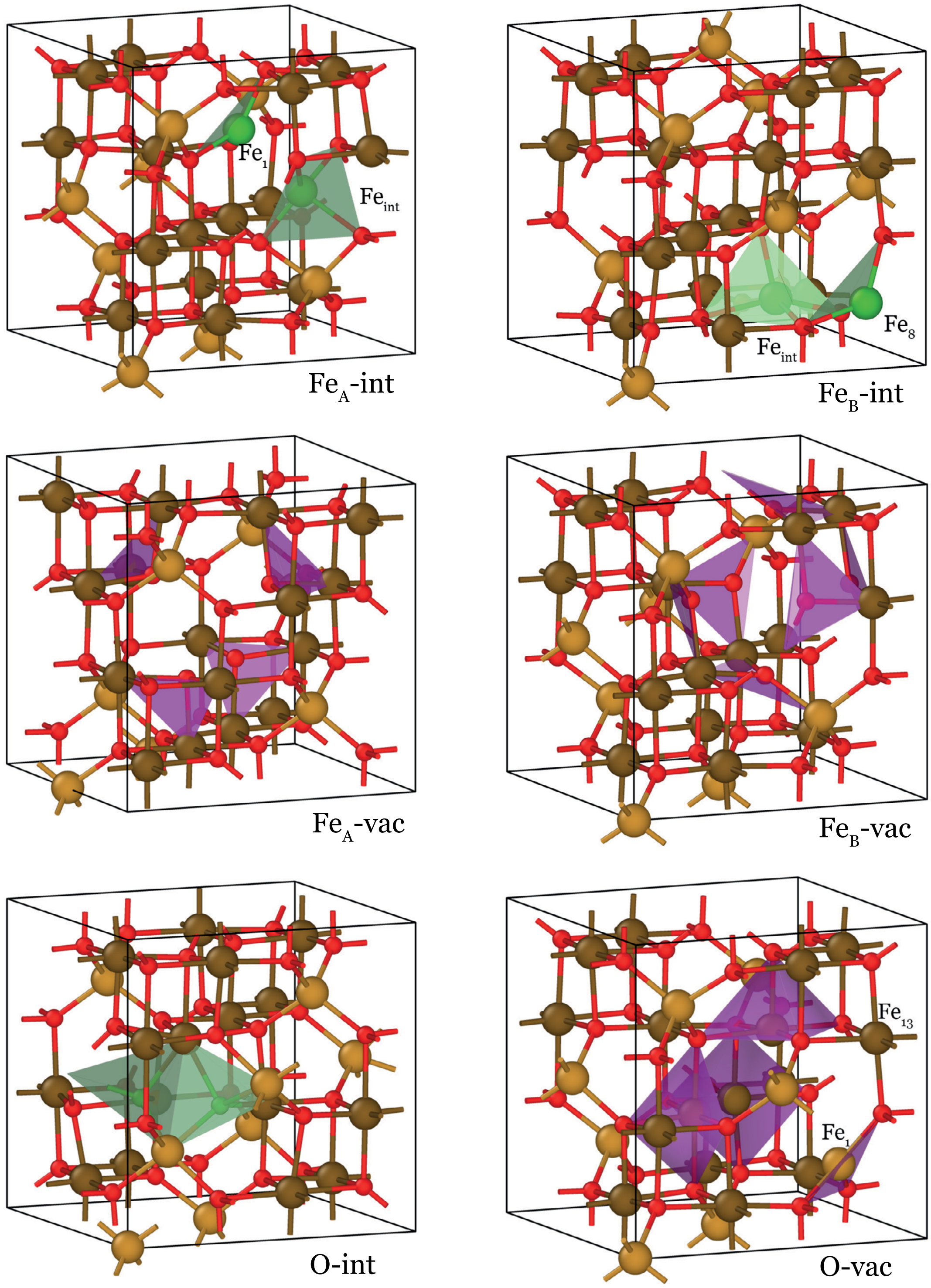

Fig. 5. (56±1)-atom cells Fe_3O_4 with a defect after relaxation. Atoms FeB are shown in brown, FeA — in sandy, O — in red; interstitials — in green, vacancy surroundings — in purple

(5) in our work. The magnitudes of atomic magnetic moments in regular cation sublattices practically did not differ from their values in pure magnetite (see Table 3).

A-interstitial Fe. Relaxation of atomic coordinates of supercells with interstitials Fe_{A1} and Fe_{A2} (interstitial positions are designated according to [62]) led to structurally and energetically similar configurations (both values are given in Table 5). One of the B-atoms near the initial interstitial position leaves its site, and a dimer of Fe atoms is located at the formed B-vacancy (Fig. 5). The magnetic moment of the cell was $34\mathrm{m}_B$ (cf. [62]). Analysis of eigenvalues of occupancy matrices showed (Fig. 6) that the valence distributions in the regular B-sublattice (octahedral) of Fe atoms in both cases were represented by six trivalent and nine divalent ions with high-spin configurations and Fe_B^{3+} $t_{2g,-}^3 e_{g,-}^2$ and Fe_B^{2+} $t_{2g,-}^3 e_{g,-}^2 t_{2g,}^1-$; in the regular A-sublattice (tetrahedral) - by eight trivalent ions Fe_A^{3+} $e_-^2 t_{2,}^3-$. The interstitial dimer in B-position consists of two ions $Fe\, t_{2,-}^3 e_-^2 (t_2 + e)_-^1$, whose magnetic moments are $3.4\mathrm{m}_B$ and $3.6\mathrm{m}_B$ and are co-directed with the B-sublattice (major spin component, atoms $Fe_B(1), Fe_{int}$ This reproduces the result of work [62]. Extra --electrons localized on each of these interstitial atoms are a mixture of t_2- and e-states due to the atoms not belonging to a regular site and lacking proper tetrahedral (or octahedral) surroundings. Thus, if these two atoms are formally considered divalent (according to the d-shell filling), then the total valence $6 \times 3 + 9 \times 2 + 2 \times 2 + 8 \times 3=64$ corresponds to the total valence of oxygen atoms in the cell. Notably, this was achieved in the approximation due to the corresponding change in the number of ions Fe_B^{2+} and Fe_B^{3+}. It is also seen that formally integer magnetic moments $5\mathrm{m}_B$ for Fe_B^{3+} and $4\mathrm{m}_B$ for Fe_B^{2+} lead to a total moment of $6 \cdot 5 + 9 \cdot 4 + 2 \cdot 4 - 8 \cdot 5 = 34\ \mu B$.

B-interstitials Fe. It should be noted that the most energetically favorable configuration we found for Fe interstitial in B-site differed from that indicated in [62]: 1) the magnetic moment of the cell was not $26\mathrm{m}_B$, but $28\mathrm{m}_B$; 2) according to [62], after relaxation, the interstitial and neighboring Fe_A -atoms hardly shifted, while in our case, the atom from A-site moves to the nearest free B-interstitial position adjacent to the existing B-interstitial. Thus, the configuration after relaxation actually represented two Fe atoms in adjacent interstitial B-sites surrounding a vacancy in A-site: $2Fe_{B,int} + V_{Fe,A}$, see Fig. 5, rather than one $Fe_{B,int}$ interstitial.. Such configuration was obtained during relaxation for the magnetic moment $26\mathrm{m}_B$ as well, but we found that cells with magnetic moment $26\mathrm{m}_B$ had higher energies both at atomic coordinates obtained for $28\mathrm{m}_B$, and at configuration similar to [62], i.e., additional energy gain was acquired precisely considering the new redistribution of electrons on Fe d-shells. Analysis of $3d$-orbital occupancy matrices showed (Fig. 6) that the regular B-sublattice of Fe atoms in the cell contains sevenFe_B^{3+} $t_{2g,-}^3 e_{g,-}^2$ ions and 9 Fe_B^{2+} $t_{2g,-}^3 e_{g,-}^2 t_{2g,}^1-$, ions, while A-sublattice contains seven Fe_A^{3+} $t_{2,}^3 - e_-^2$. ions. Two B-interstitials around the A-vacancy (atoms $Fe_A(8), Fe_{int}$) have configurations practically corresponding to high-spi Fe_B^{2+} $t_{2g,}^3 - e_{g,}^2 - t_{2g,-}^1$,- $3.7\mathrm{m}_B$, but with a small admixture of $e_{g,-}$-states to $t_{2g,-}$-states (again, apparently due to distortions of the octahedral environment); magnetic moments are oriented antiparallel to B-sublattice. In [62], the magnetic moment of (one) B-interstitial was - $3.73\mathrm{m}_B$, also antiparallel to B-sublattice, but the distribution of charge states $10\,Fe_B^{2+}$, $6\,Fe_B^{3+}$, $8\,Fe_A^{3+}$ and Fe_{int}^{2+} also 64, which corresponds to the sum of oxygen valences, with a magnetic moment of $10 \times 4 + 6 \times 5 - 8 \times 5 - 4 = 26\mathrm{m}_B$, while in our configuration with two interstitials in B-sites and A-vacancy: $9\,Fe_B^{2+}$, $7\,Fe_B^{3+}$, $7\,Fe_A^{3+}$ and $2\,Fe_{B,int}^{2+}$ — also 64, which corresponds to the sum of oxygen valences, with a magnetic moment of $9 \times 4 + 7 \times 5 - 7 \times 5 - 2 \times 4 = 28\mathrm{m}_B$. Naturally, as in the case of A-interstitial, divalent ions increase while trivalent ions decrease, but in this case, the change in proportion is partly related to the transition of tetrahedral trivalent iron atom to divalent state with almost octahedral environment.

A- and B-vacancies of Fe. No significant structural changes were observed after relaxation of cells with a single iron vacancy in Fe_3O_4, except for a slight repulsion of oxygen atoms from the vacancy location (see Fig. 5). The B-vacancy has a lower formation energy than the A-vacancy (see Table 5), and the magnetic moments of the cell are and respectively, where highspin configurations of ions are implied; the change in the ratio of divalent and trivalent iron atoms exactly compensates for the disappearance of one iron atom (Fig. 6); similar results were obtained in [61].

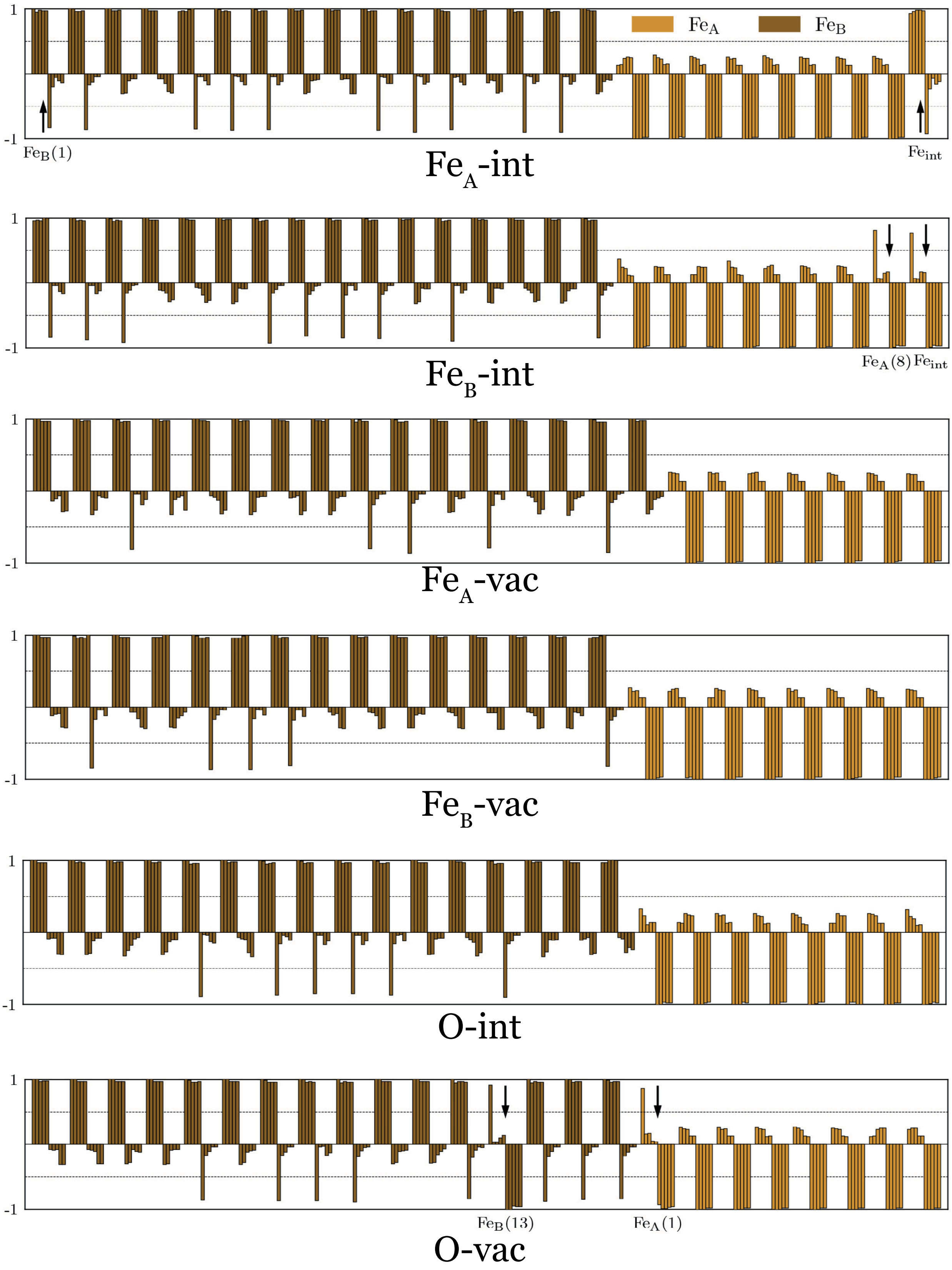

Fe_A-int

Fe_B-int

Fe_A-vac

Fe_B-vac

O-int

O-vac

Fig. 6. Eigenvalues of occupation matrices of 3*d*-shells Fe_B (brown) and Fe_A (sandy) in (56±1)-atom cells Fe_3O_4, see Fig. 5. Arrow positions are explained in the text

O vacancies and interstitials. During calculations, it was found that the DFT+U method applied to structures $\mathrm{Fe_{24}O_{32\pm1}}$, containing oxygen point defects led to a particularly wide variety of possible magnetic and charge orderings (especially finely pitted with minima energy surface of the orbital-dependent Hubbard contribution), since configurations with similar energies included both those that differed in the $\mathrm{Fe_B}$ position of the $\mathrm{Fe_B}$ atoms, with their valence states changed, relative to the defect, and those where spin flip of one of the atoms $30\mathrm{m}_B$ ($5\,\mathrm{Fe_B^{2+}}, 10\,\mathrm{Fe_B^{3+}}, 8\,\mathrm{Fe_A^{3+}}$) and $40\mathrm{m}_B$ ($5\,\mathrm{Fe_B^{2+}}, 11\,\mathrm{Fe_B^{3+}}, 7\,\mathrm{Fe_A^{3+}}$) in our notation), and (in the case of vacancy) change in valency of atom $\mathrm{Fe_A}$ from 3 to 2. We limited ourselves to a semi-intuitive search through a sufficiently large number (about 10–15) of initial orderings, realizing that covering such a large configurational space of possible spin and charge ordering combinations is extremely difficult, but noting that we were able to localize the desired ground state energies within no more than 50 meV from the lowest energies we found for structures with oxygen vacancy or interstitial.

Thus, in the case of an interstitial (see Fig. 5), the spin reversal of the octahedral Fe atom and the valence change of the tetrahedral one proved unfavorable, with the final structure having valence distribution and high-spin configurations according to $6\,\mathrm{Fe_B^{2+}}\ t^3_{2g,-}e^2_{g,-}t^1_{2g,}$-, $10\,\mathrm{Fe_B^{3+}}\ t^3_{2g,-}e^2_{g,-}$, $8\,\mathrm{Fe_A^{3+}}\ e^2_{-}t^3_{2,}$- Fig. 6) the total moment of $6\times4+10\times5-8\times5=34\mathrm{m}_B$. Changes in cation positions were not as significant, but one of the neighboring O atoms shifted noticeably and occupied a position in the tetrahedral cation environment $2\mathrm{Fe_A}+2\mathrm{Fe_B}$) symmetrically to the interstitial O atom relative to the diagonal chain of atoms $\mathrm{Fe_B}$, becoming indistinguishable from the interstitial itself.

The appearance of an O vacancy (see Fig. 5) makes configurations in which the $\mathrm{Fe_B}$ atoms closest to the vacancy are predominantly divalent most favorable (see Fig. 6), as the excess electron density due to uncompensated valences was well localized on the cations $\mathrm{Fe_B^{2+}}$. In the lowest-energy structure found in this work, all 6 ions corresponded to the configuration $\mathrm{Fe_B^{2+}}$. Additionally, one of the atoms nearest to the vacancy $\mathrm{Fe_B}$, connected to the vacancy-adjacent $\mathrm{Fe_A}(1)$ atom by an oxygen bridge, changed its spin projection ($\mathrm{Fe^{2+}_{B,}}$-, $\mathrm{Fe_B}(13)$ in Fig. 6). The cation itself $\mathrm{Fe_A}(1)$, deprived of a bond with one oxygen atom, became divalent ($\mathrm{Fe^{2+}_{A,}}-e^2_{-}t^3_{2,}-t^1_{2,-}$), with the excess electron localized on t_2-orbitals with equal contribution from each $\left((1/\sqrt{3})(d^-_{xy}+d^-_{xz}+d^-_{yz})\right)$. In the entire B-sublattice overall, there was also one more divalent ion (high-spin $7\mathrm{Fe_B^{3+}}, 9\mathrm{Fe}_B^{2+}$). The total magnetic moment of the cell was $8\times4+7\times5-4-4-7\times5=24\mathrm{m}_B$. The excess electron density at the vacancy site was thus redistributed as two additional electrons localized on the neighboring $\mathrm{Fe_A}$ and $\mathrm{Fe_B}$, Fig. 10, top. This explains the displacement (repulsion) of the atom $\mathrm{Fe_A}$ away from the vacancy location, so that it is practically in the plane of the three remaining neighboring O atoms (in trigonal coordination), as clearly seen by the almost flat coordination $\mathrm{Fe_A}$ polyhedron in Fig. 5.

6.2.2. Chromite

In chromite, as seen from the right part of Table 3, under oxygen excess conditions, chromium vacancies form most easily. Under oxygen deficiency conditions, oxygen vacancies and antisites form most easily. Interstitials, both Fe and Cr, as well as O, are the most difficult to form.

Cr and Fe interstitials. The final structure with Cr interstitial with the lowest energy resembled the result for B interstitial in $\mathrm{Fe_3O_4}$ after relaxation, specifically, the Fe atom adjacent to the Cr interstitial shifted almost to the neighboring B interstitial position, while the Cr interstitial itself occupied another adjacent B interstitial position (compare Fig. 5 and 7). The magnetic moments of two Cr atoms — the interstitial itself and the neighboring regular B atom (Cr_{int} and Cr(2) in Fig. 8, respectively) — differ from those possessed by atoms $\mathrm{Cr_B^{3+}}\ t^3_{2g,-}e^0_{g,-}$ in regular lattice sites (see Table 4): it equals $4.0\mathrm{m}_B$ for the interstitial Cr_{int} and $3.6\mathrm{m}_B$ for the neighboring atom Cr(2). Judging by the occupation matrices (Fig. 8), these atoms can be associated with valence states $\mathrm{Cr^{1+}}\ t^3_{2g,-}e^2_{g,-}$, $\mathrm{Cr^{2+}}\ t^3_{2g,-}e^1_{g,-}$ and nominally integer magnetic moments $5\mathrm{m}_B$ and $4\mathrm{m}_B$. The displaced Fe atom, being in an environment close to octahedral, practically had configuration $\mathrm{Fe^{2+}}\ t^3_{2g,}-e^2_{g,}-t^1_{2g,-}$ (other atoms Fe — $\mathrm{Fe}_A^{2+}\ e^2_{-}t^3_{2,}-e^1_{-}$). The total magnetic moment of the cell was $5+4+15\cdot3-8\cdot4=22\ \mu_B$ ($1+2+15\cdot3+8\cdot2=64$).

In the case of Fe interstitial, however, the configuration ($2\mathrm{Fe_{B,int}}+V_{\mathrm{Fe,A}}$) no longer had the lowest energy, although it was within 0.1 eV from

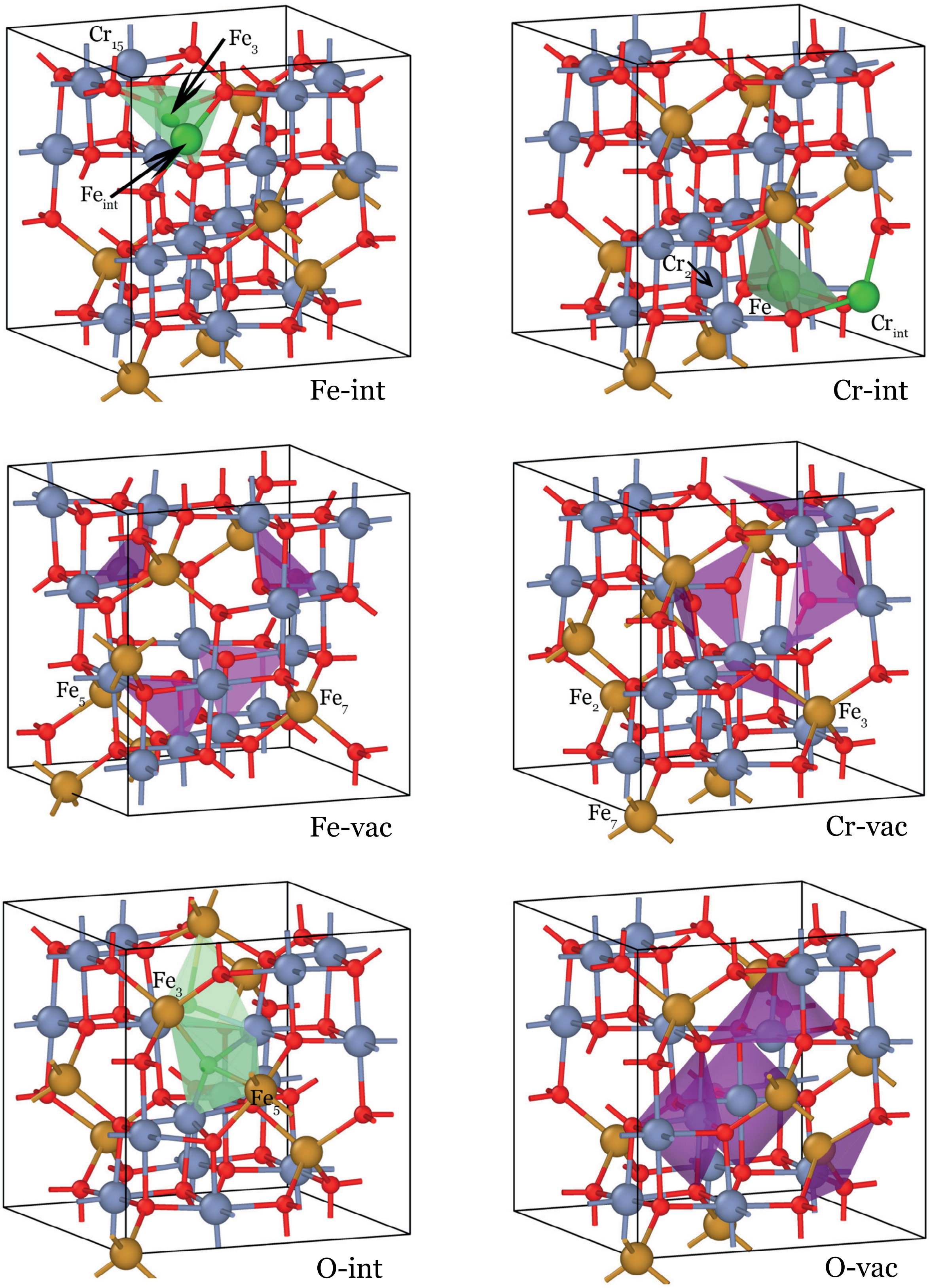

Fig. 7. (56±1)-atom cells $FeCr_2O_4$ with defect after relaxation. Atoms Cr_B are shown in sandy, Fe_A in blue, O in red; interstitials in green, vacancy surroundings in purple

it. The configuration with A2-type interstitial was more favorable (see Fig. 7); the interstitial atom was displaced from the initial A2 position towards the neighboring A-position and displaced the neighboring regular atom Fe_{int} was displaced from the initial A2 position towards the neighboring A-position and displaced the neighboring regular atom Fe_A closer to the adjacent B-interstitial position. As a result, the e_--electron peak of this Fe_A atom in the valence band maximum region (see Fig. 4) transformed into a hybrid of e-and t_2-electrons with occupation numbers closer to half (Fe(3) atom in Fig. 8, its magnetic moment ($-$ $3.5m_B$) is less than that of Fe_A^{2+}), which could affect the high formation energy of the interstitial. Similar situation arose with the interstitial itself, but with more obvious electron localization Fe_{int} (atom in Fig. 8); the interstitial had a magnetic moment $-$ $3.1m_B$, formally corresponding to state Fe_{int}^{1+}. The Cr atom neighboring the interstitial also decreased its valence and increased its magnetic moment (Cr_B^{2+}, $t_{2g,-}^3\, e_{g,-}^1$, atom Cr(15) in Fig. 8 $m = 3.6m_B$). The total integer magnetic moment was equal to $15 \times 3 - 8 \times 4 - 3 + 4 = 14m_B$ ($15 \times 3 + 8 \times 2 + 1 + 2 = 64$).

Analysis of DOS in structures with interstitials showed that additional electrons on Fe^{1+}, Cr^{1+}, Cr^{2+} atoms were strongly delocalized and led to the appearance of wide bands with strong hybridization in the majority (for spin "up") spin component in the band gap of defect-free chromite. In the case of a Cr interstitial, these bands were sufficiently close to the initial level of the conduction band minimum and led to the metallization of the band structure. They consisted $e_{g,-}$-atoms Cr^{2+} (atom Cr(2)) and $e_{g,-}$-orbitales atom Cr^{1+} (atom Cr_{int}), hybridized with $e_{g,-}$-orbitals of the remaining atoms. Cr_B^{3+}. In the case of Fe interstitial, metallization did not occur, but there was delocalization of $e_{g,-}$-electron Cr_B^{2+} (atom Cr(15)) and $t_{2,-}$-interstitial electron Fe^{1+} (atom Fe_{int}), hybridized with e_g-orbitals of Cr_B^{3+} atoms and other states.

Cr and Fe vacancies. When cation vacancies appeared, only the Fe cation sublattice responded to the change in valence balance through hole localization. Thus, in a cell with Fe vacancy (see Fig. 7), the hole density was localized on two Fe_A^{2+} atoms. For atoms Fe(5) and Fe(7) in Fig. 8, the occupation numbers of d-shells changed accordingly (Fe_A^{3+} $e_-^2\, t_{2,}^3-$, while other atoms have sual high-spin configurations Fe_A^{2+} $e_-^2\, t_{2,}^3 - e_-^1$ and Cr_B^{3+} $t_{2g,-}^3\, e_{g,-}^0$). The magnetic moment of the cell was $16 \times 3 - 5 \times 4 - 2 \times 5 = 18m_B$ ($16 \times 3 + 5 \times 2 + 2 \times 3 = 64$). In a cell with a Cr vacancy (see Fig 7.2), similarly, three atoms appeared Fe_A^{3+} (atoms in Fig. 8), with a cell Fe(2), Fe(3), Fe(7), magnetic moment of — $15 \times 3 - 5 \times 4 - 3 \times 5 = 10m_B$ ($15 \times 3 + 5 \times 2 + 3 \times 3 = 64$). The corresponding DOS changes in both cases include the appearance of unfilled e_--levels peaks of Fe_A^{3+} atoms in the middle of the band gap (forming new conduction band minimum) and right above them — peaks of unfilled $t_{2,-}$. In section 7, the more favorable position of acceptor defects (cation vacancies and oxygen interstitials) in terms of their formation energies in chromite will be discussed.

Antisite defect Fe–Cr. As a model of an antisite defect, we only consider the case when the nearest Fe and Cr atoms (connected through an O atom, (Fig. 9) exchange positions. Among several variants of magnetic and charge ordering, the cell with a magnetic moment of $16m_B$, as in defect-free magnetite, and without changes in spin projections of atoms Fe_{Cr} and Cr_{Fe}, which exchanged positions (atoms Cr_{Fe}, Fe_{Cr} in Fig. 8), had the lowest energy. However, it can be seen that the iron atom in the antisite defect became trivalent (Fe_B^{3+} $t_{2g,}^3 - e_{g,}^2-$), and chromium — became divalent (Cr_A^{2+} $e_-^2\, t_{2,-}^2$). The conduction band minimum level significantly decreased and corresponded to the freed $t_{2g,-}$-orbitals atom Fe_{Cr}, in , conversely, became higher and consisted of $t_{2,-}$-orbitals of the tetrahedral atom Cr_{Fe}. Thus, the band gap became approximately twice narrower. The order of e_g- and t_{2g}-orbitals of bothк Fe_{Cr}, and Cr_{Fe} relative to each other also changed in accordance with the modified oxygen environment. The remaining lattice atoms were in their usual electronic configurations.

O vacancies and interstitials. The oxygen interstitial configuration was the same as in Fe_3O_4, see Fig. 7, i.e., the interstitial and regular O atoms were symmetrically positioned relative to the initial regular position after relaxation. As in the case of Fe and Cr vacancies, hole density localization occurred on the atoms of Fe-sublattice. The atoms Fe(3), Fe(5), having one more oxygen neighbor than in the usual tetrahedral environment, increased their oxidation state to +3 (see Fig. 8). Due to the appearance of two Fe_A^{3+}-atoms, peaks of unfilled e_--orbitals appeared in the band gap of the majority DOS component of $FeCr_2O_4$, forming

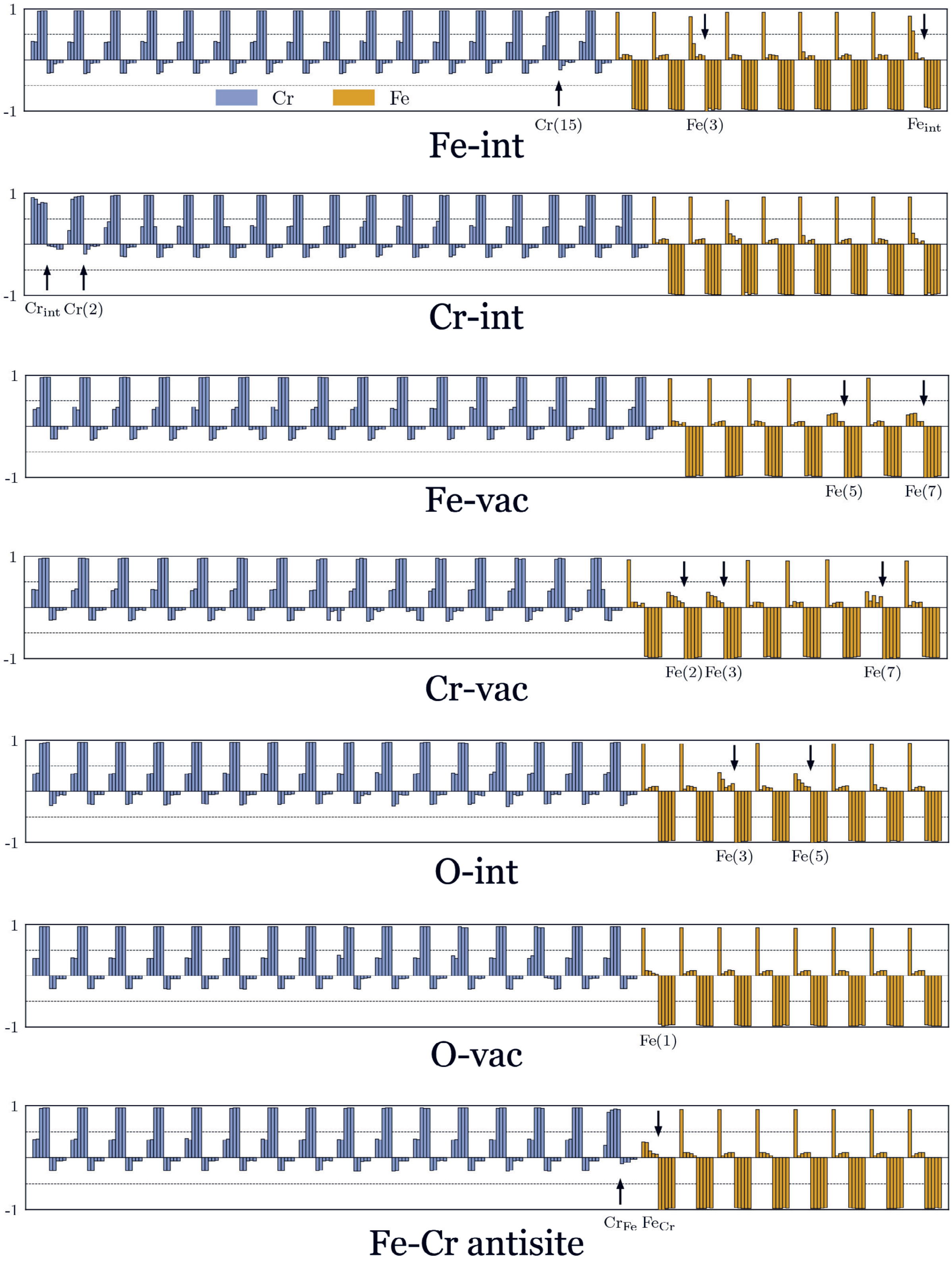

Fig. 8. Eigenvalues of occupation matrices for 3*d*-shells of Cr (blue) and Fe (sandy) in (56 ± 1)-atom cells $FeCr_2O_4$, see Fig. 7 and Fig. 9. Arrow positions are explained in the text

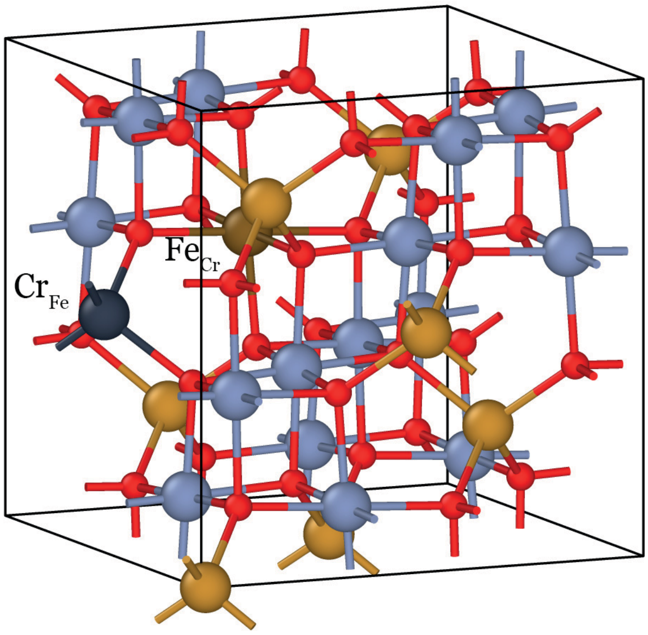

Fig. 9. 56-atom cell $FeCr_2O_4$ with an Fe-Cr antisite defect after relaxation. Antisite defect atoms (Fe_{Cr}, Cr_{Fe}) are shown in darker shades

the conduction band minimum, and above them — peaks of unfilled $t_{2,-}$-orbitals.

However, the structure with O-vac vacancy fundamentally differed from that in Fe_3O_4. Specifically, the $Fe_A(1)$, ion, deprived of a neighboring O atom and in Fe_3O_4 shifted diagonally away from the vacancy, in $FeCr_2O_4$ moved, conversely, towards the vacancy (compare Fig. 5 and 7). While in $Fe_3O_4 + V_O$ here were two more Fe^{2+} cations, in $FeCr_2O_4 + V_O$ no noticeable changes in the occupation numbers of -orbitals compared to defect-free chromite occurred, see Fig. 8, and the total magnetic moment of the cell $16m_B$ remained unchanged. A similar result was obtained for neutral O vacancies in Fe_3O_4, $CoFe_2O_4$, $NiFe_2O_4$ [59, 119, 120]. Nevertheless, in the band gap of $FeCr_2O_4 + V_O$ two new small peaks appeared, forming the valence band maximum and conduction band minimum. They belonged mostly to e_g-states of the three Cr cations nearest to the vacancy, with a noticeable admixture of 3*d*-states of other Cr atoms. To understand why configurations with a cell magnetic moment of $18m_B$, where two extra electrons were practically localized on two cations,Cr^{2+}, were less energetically favorable, and to determine how the excess charge density redistributed at the oxygen vacancy site, we visualized it in the DOS energy range that contained the peaks caused by O-vacancy appearance (approximately from - 0.5 to 0 eV relative to the valence band top). The result is shown in Fig. 10, bottom, which also includes filled e_--states Fe_A^{2+}, close to the valence band top. For comparison, the charge density of t_{2g}-states Fe_B^{2+} near the valence band maximum of $Fe_3O_4 + V_O$ is shown in Fig. 10, top. The opposite nature of atomic displacements of Fe_A (atoms No. 1 in Fig. 6 and 8) now becomes clear, since in $Fe_3O_4 + V_O$ the excess electron density is distributed over well-localized orbitals of cations Fe_A^{2+} (1) and Fe_B^{2+}, and $FeCr_2O_4 + V_O$ it is delocalized in the vacancy region between the nearest Cr atoms and Fe atom and represents a single bonding orbital consisting of hybridized e_g-states of Cr and t_{2g}-states of Fe(1). A similar electron density distribution was demonstrated for neutral O vacancy in $NiFe_2O_4$ [120]. The bonding nature of this shared orbital leads to attraction of Fe(1) to the vacancy. In contrast, in the structure with a cell magnetic moment of $18m_B$ with high degree of electron localization on Cr atoms, repulsion of Fe(1) from the vacancy was observed, as in $Fe_3O_4 + V_O$.

7. DISCUSSION

The main result of this work is the calculated formation energies of neutral point defects in magnetite and chromite. In both spinels under O_2 excess conditions, vacancies in the octahedral sublattice of metal atoms are formed most easily, while under deficiency conditions, oxygen vacancies and interstitials have the lowest and highest formation energies, respectively. It is noteworthy that in the case of magnetite, the boundary values of oxygen chemical potential practically coincide with those at which the formation energies of point defects first become zero (in our case, Fe_B or O vacancies), while this is not observed in chromite. The reason may be that charged point defects were not taken into account in this work. This might lead to overestimated formation energies, as the role of charged defects is more pronounced in $FeCr_2O_4$, than in Fe_3O_4. At the same time, in magnetite, these energies (1.21 eV for B-sublattice and 3.32 eV for A-sublattice) well reproduce the low- and high- temperature limits of activation energy for the Frenkel constant from Dieckmann et al. [89,91] (1.38 and 3.11 eV respectively). In [62], it was proposed to interpret the existence of these limits as a transition from the predominant mechanism of pair formation in B-sublattice at lower temperatures to A-pairs at higher temperatures. Since our refined value of 1.21 eV is lower than 1.38 eV from Dieckmann et al. (unlike 1.52 eV in [62]), it is additionally worth noting that our results of 1.21 and 3.32 eV differ by approximately 0.2 eV from Dieckmann et al.'s results. This may be due to the fact that the authors described the behavior of the vacancy equilibrium constant with a single exponent, unlike $K_I = K_{I¢} + K_{I¢¢}$, and due to such averaging, their results are slightly closer to each other than ours.

We have not found experimental studies of point defects in $FeCr_2O_4$, however, a comparative analysis of non-stoichiometry d in magnetite $Fe_{3-d}O_4$ [87] and mixed spinels $(Fe_{1-x}Cr_x)_{3-d}O_4$ at x £ 0.5 [92] at 1200 °C showed that increasing chromium content narrowed the range of values by approximately an order of magnitude on each side. The trends observed with increasing Cr content in $(Fe_{1-x}Cr_x)_{3-d}O_4$ are in agreement with our results for $FeCr_2O_4$.

Indeed, in chromite, the formation energies of neutral point defects are generally notably higher regardless of external conditions (oxygen activity). For adequate comparison of formation energies of point defects of the same type in two spinels, Table 6 shows the difference in formation energies

$$\mathrm{D}E_{form} = E_{form,i}(\mathrm{FeCr_2O_4}) - E_{form,i}(\mathrm{Fe_3O_4}),$$

where i is the defect type index, calculated for the same external conditions for O and Fe. This means that the chemical potential values m_i of elements are chosen on the coexistence line of Fe_3O_4 and $FeCr_2O_4$ (orange line in Fig. 3), thus eliminating the dependence $\mathrm{D}E_{form}$ on the choice of external conditions. For defects involving atoms of the same type, this is trivial since the chemical potentials in the formula above cancel each other out, and for B-sublattice defects, the resulting difference $m_{Cr} - m_{Fe}$ is a constant value independent of the chosen chemical potential values. All values in Table 6 are positive. We suggest that lower formation energies in Fe_3O_4 are a direct consequence of effective screening of electronic density perturbations in magnetite caused by defect appearance through changing the ratio of cations Fe_B^{2+} and Fe_B^{3+}. This was pointed out by Dieckmann et al., justifying the ability of cationic point defects to form an ideal-like solution in Fe_3O_4 due to high buffering capacities of the cation sublattice [87]. A similar effect was observed in the results of this study and works [61, 62, 99]. In defect-free chromite, Fe cations have a charge state of +2, and exclusively +3, the strong stabilization of the latter by the crystal field was indicated by the authors of work [121]. The appearance of cation interstitials and an oxygen vacancy led to either oxidation states unusual for Fe and Cr in iron-chromium spinels Fe(+1), Cr(+1), Cr(+2) or delocalization of released valence electrons.

Unlike Fe_3O_4, screening of excess charge density in $FeCr_2O_4$ without the need to accept an uncharacteristic oxidation state is only possible in the case of cation vacancies and oxygen interstitial, when there is an increase in the oxidation state of cations Fe_A^{2+} to another characteristic for Fe in spinels, +3. These types of defects are grouped in the left part of Table 6, and indeed, the increase in formation energies for them is noticeably less than for defects of the first group (right part of Table 6). Thus, it can be assumed that the additional destabilizing contribution to defect configurations $FeCr_2O_4$ is directly related to the appearance of oxidation states uncharacteristic for Fe and Cr atoms in spinels. Note that in the experimental study at 1200 °C he effect of Fe substitution with Cr in $(Fe_{1-x}Cr_x)_{3-d}O_4$ had a stronger impact on interstitial concentrations than those of vacancies, see Fig. 5 in work [92].

Table 6. Increase in formation energies of point defects in $FeCr_2O_4$ compared to Fe_3O_4

Defect*	$\mathrm{D}E_{form}$, eV	Defect**	$\mathrm{D}E_{form}$, eV
A-*vac*	0.76	A-*int*	2.52
B-*vac*	1.45	B-*int*	5.38
O-*int*	1.32	O-*vac*	2.35

Note.
*Lower increase.
**Higher increase.

The difference in formation energy changes during the transition from Fe_3O_4 to $FeCr_2O_4$ between vacancies and cation interstitials may only be a consequence of steric factors. However, in this case, the stronger increase in formation energies for O vacancies than for interstitials is unclear (Table 6). Therefore, one cannot ignore the factor of screening

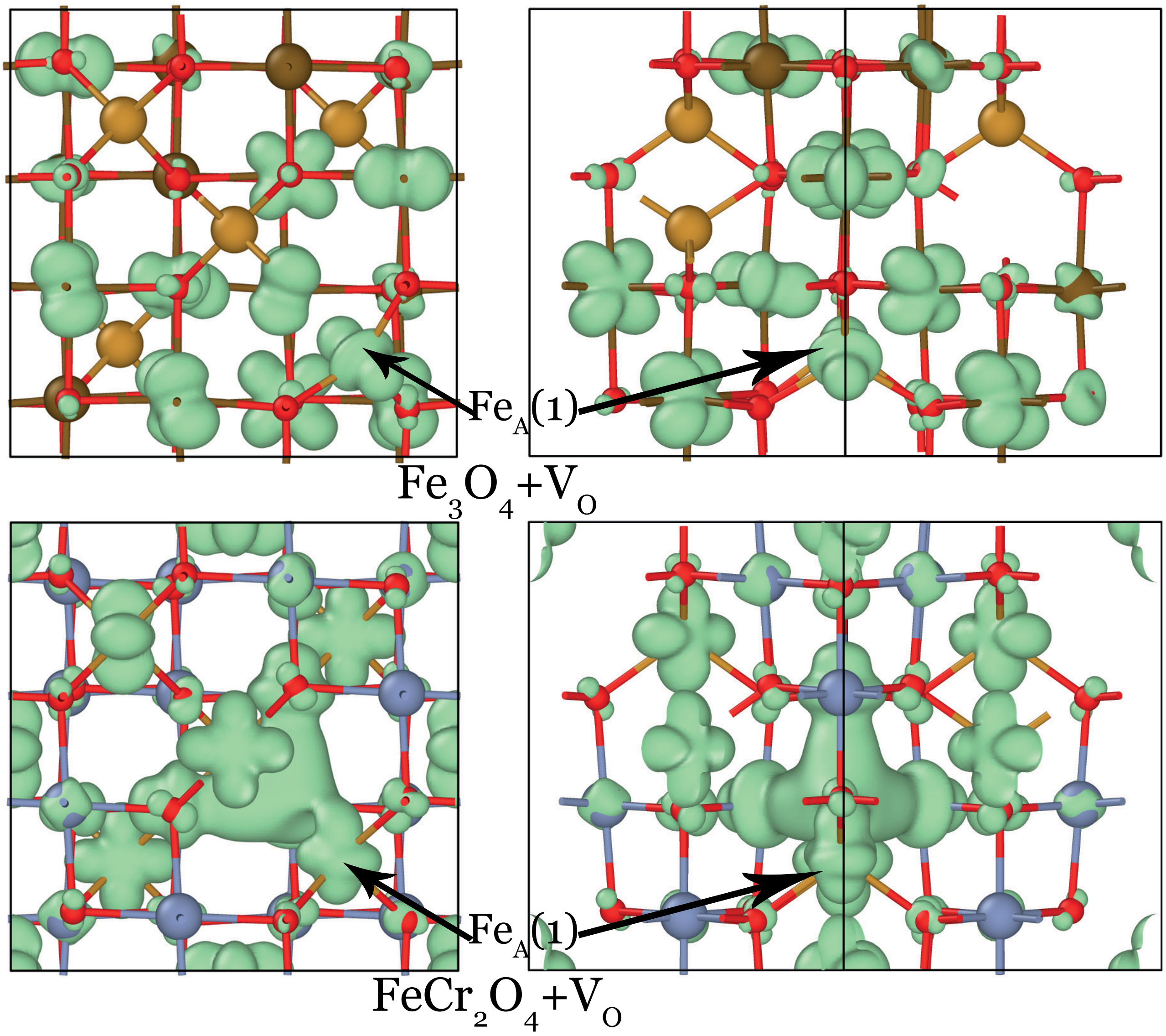

Fig. 10. Electronic density of states within 0.5 eV from the valence band top in Fe_3O_4 + VO (top) and $FeCr_2O_4$ + VO (bottom); left — [001]-projection, right — [101] -projection

ability of the Fe sublattice, which is present in $FeCr_2O_4$ as well.

The authors of work [59] examined oxygen vacancies in magnetite and studied in detail such factors affecting the formation energies of these point defects as their charge state and local ion environment Fe_B^{2+} and Fe_B^{3+}; the latter factor led to changes in the formation energies of neutral vacancies within 1.1 eV. Since the authors do not provide a specific O chemical potential for calculating formation energies, use an ordering different from Verwey's in the ground state of magnetite, and furthermore do not avoid relaxation of the defect-free cell with charge ordering, the noticeable overestimation of our result of 0.04 eV for an oxygen vacancy at the magnetite-wustite buffer to 0.8 eV in work [59] is not unexpected. Additionally, according to [59], the magnetic moment of the cell with vacancy did not change; in our case, due to the magnetic moment reversal of one of the atoms Fe_B^{2+} it decreased by $8m_B$. However, work [59] shows that among neutral configurations, the lowest energies belong to those where, firstly, one of the excess electrons is localized on the A-atom adjacent to the vacancy, and secondly, where there is no delocalization of electrons released as a result of O vacancy formation. Our configuration satisfies these conditions. A question not considered by us at this stage but deserving attention concerns the influence of spinel inversion degree and cation ratio on point defect formation energies [119, 120, 122].

It is known, however, that in magnetite, the inversion parameter, close to unity at low temperatures, decreases to zero both as some iron atoms are replaced by chromium atoms in chromite $FeCr_2O_4$, and with increasing temperature [123, 124]. In the second case, as shown for stoichiometric Fe_3O_4 [125], the resulting cationic disorder is associated not only with self- doping of magnetite (hole doping of B-sublattice) and rightward equilibrium shift:

$$Fe_B^{2+} + Fe_A^{3+} \rightleftharpoons Fe_B^{2+} + Fe_A^{3+}$$

but also with an increase in the ratio of Fe atom concentrations in B- and A-sites, $[Fe_B]/[Fe_A]$. Under stoichiometric conditions, this can occur as a result of preferential formation of Frenkel pairs $Fe_{B,int} / V_A$.

The difficulties described in [62] regarding the consistent interpretation of experiments [87, 89, 125] using DFT+U calculation results can now be partially resolved, as these works and our results are simultaneously in satisfactory agreement. Thus, Dieckmann et al.'s conclusion about the predominance of B-vacancies of iron in their total number [87, 89] is confirmed by the fact that formation energies of A-vacancies in our calculations are higher by 1.12 eV, and cannot be refuted in [125], since it investigated stoichiometric magnetite. On the other hand, the result from [125] about the increase in occupied B-sites and decrease in occupied A-sites with temperature rise is confirmed by Dieckmann et al.'s result [89] about the increase in A-vacancy fraction with temperature rise. However, it's worth noting that measurements in [125] were conducted at lower temperatures than Dieckmann et al.'s measurements. Finally, this last fact is confirmed by our results, which is not obvious at first glance. Indeed, in works [87,89] it was found that the formation regime (and migration) of cation interstitials is biexponential and switches from one mechanism to another with temperature rise. As noted above, the corresponding activation energies for Frenkel constants (1.38 and 3.11 eV [87]) were identified in [62] with the calculated formation energies of Frenkel pairs in B- and A-sublattices (1.52 and 3.27 eV). The values obtained in our work for the same categories are 1.21 and 3.32 eV and are in good agreement with results from [87]. Within such concepts of calculating Frenkel pair formation energies, the results from [125] about preferential formation of pair $Fe_{B,int} / V_A$ are difficult to interpret, since its formation energy, according to our calculations, equals 2.33 eV, which is much higher than 1.21 eV. This contradiction, noted in [62], is resolved in our work thanks to the newly discovered configuration of B-interstitial. Section 6.2.1 indicated that it actually represents two B-interstitials adjacent to an A-vacancy, i.e., formally it is not an independent B-interstitial but a B-interstitial interacting with aFrenkel pair $Fe_{B,int} / V_A$. Consequently, the energy of 1.21 eV for the formation of a Frenkel B-pair in our work can also be attributed rather to $Fe_{B,int} / V_A$ than to $Fe_{B,int} / V_B$.

Thus, for the correct interpretation of experimental data that does not provide information about processes at the micro level (in particular, the distribution of vacancies and interstitials in Frenkel pairs according to their distance from each other) and correlating them with calculation results, it may be necessary to consider the dependence of the calculated formation energy on the distance between vacancy and interstitial. As could be seen, with simple addition of formation energies of independent vacancy and interstitial, the result for a Frenkel pair may be overestimated, but, on the other hand, relaxation of the structure with undisturbed stoichiometry and an interstitial next to a vacancy should lead to underestimated values or even the ground state, i.e., the defect-free structure.

8. CONCLUSIONS

The work attempts to connect a detailed analysis of electronic and atomic structures of point defects in magnetite and chromite based on the DFT+U method with calculation of formation energies of the considered defects in these oxides under conditions of oxygen excess and deficiency. Formation energies of native neutral point defects — cation and oxygen vacancies and interstitials — in magnetite and chromite were calculated. Special attention was paid to interpreting the results of experimental works by Dieckmann et al. as the most complete and consistent known to us, though often overlooked and underanalyzed in computational studies of point defects in magnetite and other spinels. The value of the DFT+U method, thus, was combined with the richness of experimental data available for interpretation with its help (such as formation energies of Frenkel pairs).

The performed calculations of point defect formation energies led to the following main results.

1. In both magnetite and chromite, cation vacancies and O-vacancies have the lowest formation energies under conditions of O_2 excess and deficiency respectively.

2. Formation energies of neutral point defects in $FeCr_2O_4$, are notably higher than in Fe_3O_4, which can be explained from the perspective of high buffering capacity of the mixed-valence ion system Fe^{3+}/Fe^{2+} in magnetite; this property of the iron ion system was also partially manifested in chromite during the formation of cation vacancies and an oxygen interstitial.

3. The Frenkel pair formation energies were

1.21 eV in the B-sublattice of iron in Fe_3O_4 good agreement with experimental values;

2.90 eV in the O-sublattice of magnetite;

6.62 eV in the Fe-sublattice of chromite;

6.57 eV in the O-sublattice of chromite

Comparison of the obtained calculation results for magnetite within the framework of the DFT+Umethod with experimental data from Dieckmann et al. and a recent experiment [125] indicates that when interpreting experimental results, the possibility of a composite nature of the Frenkel pair in magnetite discovered in this work should be taken into account.

FUNDING

This work was financially supported by the Ministry of Science and Higher Education of the Russian Federation (agreement with JIHT RAS No. 075-01129-23-00 dated December 29, 2022). The research was carried out within the framework of the HSE University Basic Research Program. Calculations were performed at the supercomputer centers of JIHT RAS and MIPT Department of Information Technologies. Additionally, the authors thank JSCC RAS for the provided computational resources.

REFERENCES

1. K. I. Kugel' and D. I. Khomskiĭ, Sov. Phys. Usp. 25, 231 (1982).
2. S. V. Streltsov and D. I. Khomskii, Phys-Usp. 60, 1121 (2017).
3. D. I. Khomskii and S. V. Streltsov, Chem. Rev. 121, 2992 (2021).
4. M. Y. Kagan, K. I. Kugel, and D. I. Khomskii, J. Exp. Theor. Phys. 93, 415 (2001).
5. I. I. Mazin, D. I. Khomskii, R. Lengsdorf, J. A. Alonso, W. G. Marshall, R. M. Ibberson, A. Podlesnyak, M. J. Martínez-Lope, and M. M. Abd-Elmeguid, Phys. Rev. Lett. 98, 176406 (2007).
6. A. O. Sboychakov, A. V. Rozhkov, K. I. Kugel, and A. L. Rakhmanov, JETP Lett. 112, 651 (2020).
7. A. Bosak, D. Chernyshov, M. Hoesch, P. Piekarz, M. Le Tacon, M. Krisch, A. Kozłowski, A. M. Oleś, and K. Parlinski, Phys. Rev. X 4, 011040 (2014).
8. S. V. Ovsyannikov, M. Bykov, E. Bykova, D. P. Kozlenko, A. A. Tsirlin, A. E. Karkin, V. V. Shchennikov, S. E. Kichanov, H. Gou, A. M. Abakumov, R. Egoavil, J. Verbeeck, C. McCammon, V. Dyadkin, D. Chernyshov, S. van Smaalen, and L. S. Dubrovinsky, Nat. Chem. 8, 501 (2016).
9. S. V. Ovsyannikov, M. Bykov, S. A. Medvedev, P. G. Naumov, A. Jesche, A. A. Tsirlin, E. Bykova, I. Chuvashova, A. E. Karkin, V. Dyadkin, D. Chernyshov, and L. S. Dubrovinsky, Angew. Chem. Int. Ed. 59, 5632 (2020).
10. V. I. Anisimov, I. S. Elfimov, N. Hamada, and K. Terakura, Phys. Rev. B 54, 4387 (1996).
11. V. S. Zhandun, N. V. Kazak, I. Kupenko, D. M. Vasiukov, X. Li, E. Blackburn, and S. G. Ovchinnikov, Dalton Trans. 53, 2242 (2024).
12. V. I. Anisimov, J. Zaanen, and O. K. Andersen, Phys. Rev. B 44, 943 (1991).
13. A. I. Liechtenstein, V. I. Anisimov, and J. Zaanen, Phys. Rev. B 52, R5467 (1995).
14. V. I. Anisimov, F. Aryasetiawan, and A. I. Lichtenstein, J. Phys.: Condens. Matter 9, 767 (1997).
15. V. I. Anisimov, A. I. Poteryaev, M. A. Korotin, A. O. Anokhin, and G. Kotliar, J. Phys. Condens. Matter 9, 7359 (1997).
16. G. Trimarchi, I. Leonov, N. Binggeli, D. Korotin, and V. I. Anisimov, J. Phys.: Condens. Matter 20, 135227 (2008).
17. L. Hozoi, L. Siurakshina, P. Fulde, and J. van den Brink, Sci. Rep. 1, 65 (2011).

18. S. Nishimoto, V. M. Katukuri, V. Yushankhai, H. Stoll, U. K. Rößler, L. Hozoi, I. Rousochatzakis, and J. van den Brink, Nat. Commun. 7, 10273 (2016).

19. D. A. Maltsev, Y. V. Lomachuk, V. M. Shakhova, N. S. Mosyagin, L. V. Skripnikov, and A. V. Titov, Phys. Rev. B 103, 205105 (2021).

20. A. V. Oleynichenko, Y. V. Lomachuk, D. A. Maltsev, N. S. Mosyagin, V. M. Shakhova, A. Zaitsevskii, and A. V. Titov, Phys. Rev. B 109, 125106 (2024).

21. J. Zhang, Corros. Sci. 51, 1207 (2009).

22. Q. Chen, Y. Chen, F. Zhang, J. Yang, C. Zhu, W. Zhang, H. Liu, Y. Zhong, J. Deng, Q. Li, N. Liu, and J. Yang, J. Nucl. Mater. 573, 154097 (2023).

23. N. Li and J. Zhang, Oxid. Met. 63, 353 (2005).

24. K. Lambrinou, V. Koch, G. Coen, J. Van den Bosch, and C. Schroer, J. Nucl. Mater. 450, 244 (2014).

25. L. Martinelli and F. Balbaud-Célérier, Mater. Corros. 62, 531 (2011).

26. D. Kolotinskii, V. Nikolaev, V. Stegailov, and A. Timofeev, Corros. Sci. 211, 110829 (2023).

27. Y. Li, R. Zhou, X. Long, T. Gao, and C. Chen, J. Nucl. Mater. 583, 154492 (2023).

28. D. Li, C. Song, H. Y. He, C. S. Liu, and B. C. Pan, Phys. Chem. Chem. Phys. 16, 7417 (2014).

29. D. Li, B. Qu, H. Y. He, Y. G. Zhang, Y. Xu, B. C. Pan, and R. Zhou, Phys. Chem. Chem. Phys. 18, 7789 (2016).

30. Y. Lei, Y. Zhang, X. Li, Y. Xu, X. Wu, X. Wang, M. Sun, J. Yang, C. Liu, and Z. Wang, J. Nucl. Mater. 582, 154470 (2023).

31. E. J. W. Verwey, Nature 144, 327 (1939).

32. E. J. Verwey, P. W. Haayman, and F. C. Romeijn, J. Chem. Phys. 15, 181 (1947).

33. J. E. Lorenzo, C. Mazzoli, N. Jaouen, C. Detlefs, D. Mannix, S. Grenier, Y. Joly, and C. Marin, Phys. Rev. Lett. 101, 226401 (2008).

34. G. Shirane, D. E. Cox, and S. J. Pickart, J. Appl. Phys. 35, 954 (1964).

35. S. Bordács, D. Varjas, I. Kézsmárki, G. Mihály, L. Baldassarre, A. Abouelsayed, C. A. Kuntscher, K. Ohgushi, and Y. Tokura, Phys. Rev. Lett. 103, 077205 (2009).

36. S. Nakamura and A. Fuwa, Phys. Procedia 75, 747 (2015).

37. K. Tomiyasu, H. Hiraka, K. Ohoyama, and K. Yamada, J. Phys. Soc. Jpn. 77, 124703 (2008).

38. J. A. G. Cerón, D. A. L. Téllez, and J. Roa-Rojas, J. Electron. Mater. 51, 822 (2022).

39. H.-T. Jeng, G. Y. Guo, and D. J. Huang, Phys. Rev. Lett. 93, 156403 (2004).

40. I. Leonov, A. N. Yaresko, V. N. Antonov, M. A. Korotin, and V. I. Anisimov, Phys. Rev. Lett. 93, 146404 (2004).

41. H. P. Pinto and S. D. Elliott, J. Phys. Condens. Matter 18, 10427 (2006).

42. P. Piekarz, K. Parlinski, and A. M. Oleś, Phys. Rev. Lett. 97, 156402 (2006).

43. P. Piekarz, K. Parlinski, and A. M. Oleś, Phys. Rev. B 76, 165124 (2007).

44. F. Zhou and G. Ceder, Phys. Rev. B 81, 205113 (2010).

45. P. W. Anderson, Phys. Rev. 102, 1008 (1956).

46. H.-Y. Huang, Z.-Y. Chen, R.-P. Wang, F. M. de Groot, W.-B. Wu, J. Okamoto, A. Chainani, A. Singh, Z.-Y. Li, J.-S. Zhou, H.-T. Jeng, G. Y. Guo, J.-G. Park, L. H. Tjeng, C. T. Chen, and D. J. Huang, Nat. Commun. 8, 15929 (2017).

47. M. S. Senn, J. P. Wright, and J. P. Attfield, Nature 481, 173 (2012).

48. M. S. Senn, J. P. Wright, J. Cumby, and J. P. Attfield, Phys. Rev. B 92, 024104 (2015).

49. M. S. Senn, I. Loa, J. P.Wright, and J. P. Attfield, Phys. Rev. B 85, 125119 (2012).

50. P. Piekarz, D. Legut, E. Baldini, C. A. Belvin, T. Kołodziej, W. Tabiś, A. Kozłowski, Z. Kakol, Z. Tarnawski, J. Lorenzana, N. Gedik, A. M. Oleś, J. M. Honig, and K. Parlinski, Phys. Rev. B 103, 104303 (2021).

51. W. Wang, J. Li, Z. Liang, L. Wu, P. M. Lozano, A. C. Komarek, X. Shen, A. H. Reid, X. Wang, Q. Li, W. Yin, K. Sun, I. K. Robinson, Y. Zhu, M. P. Dean, and J. Tao, Sci. Adv. 9, eadf8220 (2023).

52. J. Noh, O. I. Osman, S. G. Aziz, P. Winget, and J.-L. Brédas, Sci. Technol. Adv. Mater. 15, 044202 (2014).

53. J.-H. Park, L. H. Tjeng, J. W. Allen, P. Metcalf, and C. T. Chen, Phys. Rev. B 55, 12813 (1997).

54. D. Schrupp, M. Sing, M. Tsunekawa, H. Fujiwara, S. Kasai, A. Sekiyama, S. Suga, T. Muro, V. A. M. Brabers, and R. Claessen, Europhys. Lett. 70, 789 (2005).

55. S. K. Park, T. Ishikawa, and Y. Tokura, Phys. Rev. B 58, 3717 (1998).

56. A. Hevroni, M. Bapna, S. Piotrowski, S. A. Majetich, and G. Markovich, J. Phys. Chem. Lett. 7, 1661 (2016).

57. A. Banerjee and A. J. Pal, J. Phys.: Condens. Matter 32, 055701 (2019).

58. L. Craco, M. S. Laad, and E. Müller-Hartmann, Phys. Rev. B 74, 064425 (2006).

59. S. Srivastava, B. P. Uberuaga, and M. Asta, J. Phys. Chem. C 127, 17460 (2023).

60. H. Liu and C. Di Valentin, J. Phys. Chem. C 121, 25736 (2017).

61. M. I. Shutikova and V. V. Stegailov, J. Exp. Theor. Phys. 133, 206 (2021).

62. M. I. Shutikova and V. V. Stegailov, J. Phys.: Condens. Matter 34, 475701 (2022).

63. N. Naveas, R. Pulido, C. Marini, P. Gargiani, J. Hernandez-Montelongo, I.Brito, and M. Manso-Silván, J. Chem. Theory Comput. 19, 8610 (2023).

64. E. Gürsoy, G. B. Vonbun-Feldbauer, and R. H. Meißner, J. Phys. Chem. Lett. 14, 6800 (2023).

65. Ó. A. Restrepo, Ó. Arnache, J. Restrepo, C. S. Becquart, and N. Mousseau, Comput. Mater. Sci. 213, 111653 (2022).

66. M. Robbins, G. Wertheim, R. Sherwood, and D. Buchanan, J. Phys. Chem. Sol. 32, 717 (1971).

67. H. Levinstein, M. Robbins, and C. Capio, Mater. Res. Bull. 7, 27 (1972).

68. K. Kose and S. Iida, J. Appl. Phys. 55, 2321 (1984).

69. D. Lee and G. Chern, Physica B 407, 297 (2012).

70. J. Ma, V. O. Garlea, A. Rondinone, A. A. Aczel, S. Calder, C. dela Cruz, R. Sinclair, W. Tian, S. Chi, A. Kiswandhi, J. S. Brooks, H. D. Zhou, and M. Matsuda, Phys. Rev. B 89, 134106 (2014).

71. P. V. B. Pinho, A. Chartier, D. Menut, A. Barbier, M. O. Hunault, P. Ohresser, C. Marcelot, B. Warot-Fonrose, F. Miserque, and J.-B. Moussy, Appl. Surf. Sci. 615, 156354 (2023).

72. D. Santos-Carballal, A. Roldan, R. Grau-Crespo, and N. H. de Leeuw, Phys. Rev. B 91, 195106 (2015).

73. D. Das and S. Ghosh, J. Phys. D 48, 425001 (2015).

74. C. Li, P. Li, L. Li, D. Wang, X. Gao, and X. J. Gao, RSC Adv. 11, 21851 (2021).

75. N. A. Fominykh and V. V. Stegailov, JETP Lett. 117, 849 (2023).

76. S. A. Chambers, T. C. Droubay, T. C. Kaspar, I. H. Nayyar, M. E. McBriarty, S. M. Heald, D. J. Keavney, M. E. Bowden, and P. V. Sushko, Adv. Funct. Mater. 27, 1605040 (2017).

77. C. Benhalima, S. Amari, L. Beldi, and B. Bouhafs, Spin 9, 1950014 (2019).

78. D. A. Andersson and C. R. Stanek, Phys. Chem. Chem. Phys. 15, 15550 (2013).

79. L. Sun, J. Alloys Compd. 875, 160065 (2021).

80. T. Ramachandran and F. Hamed, Mater. Res. Bull. 95, 104 (2017).

81. A. Boudjemaa, R. Bouarab, S. Saadi, A. Bouguelia, and M. Trari, Appl. Energy 86, 1080 (2009).

82. C. Freysoldt, B. Grabowski, T. Hickel, J. Neugebauer, G. Kresse, A. Janotti, and C. G. Van de Walle, Rev. Mod. Phys. 86, 253 (2014).

83. R. Dieckmann, J. Phys. Chem. Sol. 59, 507 (1998).

84. R. Dieckmann and H. Schmalzried, Ber. Bunsenges. Phys. Chem. 81, 344 (1977).

85. R. Dieckmann and H. Schmalzried, Ber. Bunsenges. Phys. Chem. 81, 414 (1977).

86. R. Dieckmann, T. O. Mason, J. D. Hodge, and H. Schmalzried, Ber. Bunsenges. Phys. Chem. 82, 778 (1978).

87. R. Dieckmann, Ber. Bunsenges. Phys. Chem. 86, 112 (1982).

88. R. Dieckmann, C. A. Witt, and T. O. Mason, Ber. Bunsenges. Phys. Chem. 87, 495 (1983).

89. R. Dieckmann and H. Schmalzried, Ber. Bunsenges. Phys. Chem. 90, 564 (1986).

90. M. Backhaus-Ricoult and R. Dieckmann, Ber. Bunsenges. Phys. Chem. 90, 690 (1986).

91. R. Dieckmann, M. R. Hilton, and T. O. Mason, Ber. Bunsenges. Phys. Chem. 91, 59 (1987).

92. J. Töpfer, S. Aggarwal, and R. Dieckmann, Solid State Ion. 81, 251 (1995).

93. S. Aggarwal and R. Dieckmann, Phys. Chem. Miner. 29, 695 (2002a).

94. S. Aggarwal and R. Dieckmann, Phys. Chem. Miner. 29, 707 (2002b).

95. N. Peterson, W. Chen, and D. Wolf, J. Phys. Chem. Solids 41, 709 (1980).

96. J. A. Van Orman and K. L. Crispin, Rev. Mineral. Geochem. 72, 757 (2010).

97. F. Millot and N. Yan, J. Phys. Chem. Solids 58, 63 (1997).

98. S. Shousha, S. Khalil, and M. Youssef, Phys. Chem. Chem. Phys. 23, 25518 (2021).

99. C. L. Muhich, V. J. Aston, R. M. Trottier, A. W. Weimer, and C. B. Musgrave, Chem. Mater. 28, 214 (2016).

100. Y. Meng, X.-W. Liu, C.-F. Huo, W.-P. Guo, D.-B. Cao, Q. Peng, A. Dearden, X. Gonze, Y. Yang, J.Wang, H. Jiao, Y. Li, and X.-D.Wen, J. Chem. Theory Comput. 12, 5132 (2016).

101. M. W. Chase, NIST-JANAF Thermochemical Tables, ACS, New York (1998).

102. G. Kresse and J. Hafner, Phys. Rev. B 49, 14251 (1994).

103. G. Kresse and J. Furthmüller, Comput. Mater. Sci. 6, 15 (1996).

104. G. Kresse and J. Furthmüller, Phys. Rev. B 54, 11169 (1996).

105. P. E. Blöchl, Phys. Rev. B 50, 17953 (1994).

106. J. P. Perdew, K. Burke, and M. Ernzerhof, Phys. Rev. Lett. 77, 3865 (1996).

107. P. E. Blöchl, O. Jepsen, and O. K. Andersen, Phys. Rev. B 49, 16223 (1994).

108. S. L. Dudarev, G. A. Botton, S. Y. Savrasov, C. J. Humphreys, and A. P. Sutton, Phys. Rev. B 57, 1505 (1998).

109. V. Stegailov, G. Smirnov, and V. Vecher, Concurr. Comput. Pract. Exp. 31, e5136 (2019).

110. A. Stukowski, Model. Simul. Mater. Sci. Eng. 18, 015012 (2010).

111. S. P. Ong, W. D. Richards, A. Jain, G. Hautier, M. Kocher, S. Cholia, D. Gunter, V. L. Chevrier, K. A. Persson, and G. Ceder, Comput. Mater. Sci. 68, 314 (2013).

112. I. Mosquera-Lois, S. R. Kavanagh, A. Walsh, and D. O. Scanlon, J. Open Source Softw. 7, 4817 (2022).

113. I. Mosquera-Lois, S. R. Kavanagh, A. Walsh, and D. O. Scanlon, Npj Comput. Mater. 9, 1 (2023).

114. S. E. Ziemniak, L. M. Anovitz, R. A. Castelli, and W. D. Porter, J. Chem. Thermodyn. 39, 1474 (2007).

115. R. Snethlage and D. Klemm, Neues Jb. Miner. Abh. 125, 227 (1975).

116. M. Shevchenko, D. Shishin, and E. Jak, Ceram. Int. 48, 33418 (2022).

117. B. Dorado, B. Amadon, M. Freyss, and M. Bertolus, Phys. Rev. B 79, 235125 (2009).

118. B. Meredig, A. Thompson, H. A. Hansen, C. Wolverton, and A. van de Walle, Phys. Rev. B 82, 195128 (2010).

119. K. Sharma, L. Calmels, D. Li, A. Barbier, and R. Arras, Phys. Rev. Mater. 6, 124402 (2022).

120. R. Arras, K. Sharma, and L. Calmels, J. Mater. Chem. C 12, 556 (2024).

121. H. S. C. O'Neil and A. Navrotsky, Am. Mineral. 69, 733 (1984).

122. R. Eppstein and M. Caspary Toroker, ACS Mater. Au. 2, 269 (2022).

123. V. A. Kurepin, Contrib. Mineral. Petrol. 149, 591 (2005).

124. D. Levy, R. Giustetto, and A. Hoser, Phys. Chem. Miner. 39, 169 (2012).

125. H. Elnaggar, S. Graas, S. Lafuerza, B. Detlefs, W. Tabiś, M. A. Gala, A. Ismail, A. van der Eerden, M. Sikora, J. M. Honig, P. Glatzel, and F. de Groot, Phys. Rev. Lett. 127, 186402 (2021).